Tectonophysics 837 (2022) 229434



Contents lists available at ScienceDirect

Tectonophysics

journal homepage: www.elsevier.com/locate/tecto





Seismic sources of InSight marsquakes and seismotectonic context of Elysium Planitia, Mars

A. Jacob [a,*], M. Plasman [a], C. Perrin [b], N. Fuji [a], P. Lognonné [a], Z. Xu [a], M. Drilleau [c], N. Brinkman [d], S. Stähler [d], G. Sainton [a], A. Lucas [a], D. Giardini [d], T. Kawamura [a], J. Clinton [d], W.B. Banerdt [e]

[a] Université de Paris, Institut de physique du globe de Paris, CNRS, F-75005 Paris, France
[b] Nantes Université, Université d'Angers, Le Mans Université, CNRS, UMR 6112, Laboratoire de Planétologie et Géosciences, UAR 3281, Observatoire des Sciences de l'Univers de Nantes Atlantique, Nantes, France
[c] 1Institut Supérieur de l'Aéronautique et de l'Espace ISAE-SUPAERO, 10 Avenue Edouard Belin, 31400 Toulouse, France
[d] Institute of Geophysics, ETH Zürich, Zürich, Switzerland
[e] Jet Propulsion Laboratory, California Institute of Technology, 4800 Oak Grove Drive, Pasadena, CA 91109, USA

ARTICLE INFO

Keywords:
InSight mission
Mars
Cerberus fossae
Moment tensors

ABSTRACT

Since early 2019, the InSight mission has proven that Mars is seismically active, with more than 900 seismic events recorded. Among them, several events have characteristics close to terrestrial tectonic earthquakes. Most of these events are located on the major graben system of Cerberus fossae and, a little further north, on the secondary system of Grjotá Valles. In this study, we invert the seismic moment tensors for nine of these tectonic marsquakes characterized by high quality data. Seven of them are located on Cerberus fossae/Grjotá Valles and two of them are located near the Martian dichotomy. The moment tensors allow us to interpret the nature and depth of the seismic sources at the origin of these events. In our approach, we invert the P and S body waveforms, the PP, SS, PPP and SSS secondary phase maximum amplitudes and we look for solutions with surface waves weaker than the Martian noise. From our results on moment tensors, we determine that all our events have been triggered at moderate depths of 15–36 km. We deduce that the seven events located on Cerberus fossae have geometries similar to the fractures and are generated by tectonics. This activity is supposed to result from the reactivation of previous faults and fractures, which would have been initially induced by the propagation of volcanic dikes at depth. The two dichotomy events are due to deep compressive fracturing of the Martian lowlands. They are therefore triggered by the planetary thermal contraction. Our results are in strong agreement with recent studies on the event depths and on the previous moment tensors calculated for two events.

1. Introduction

The NASA InSight (Interior Exploration using Seismic Investigations, Geodesy and Heat Transport, Banerdt et al, 2020) mission landed on November, 26*th* 2018 on Elysium Planitia, Mars. The mission is dedicated to study the interior of Mars through seismology and heat flux. The main instrument, the seismometer SEIS (Seismic Experiment for Interior Structure, Lognonné et al, 2019, 2020) has successfully been deployed in January 2019 and it has been continuously recording the seismic activity of Mars since February 2019. The recorded seismic data have shown that Mars is seismically active with more than 900 "marsquakes" detected in the v9 catalog released by the InSight Marsquake Service (MQS) which covers events detection until 2022/01/01. For more details on the MQS catalogs, see Giardini et al (2020), InSight Marsquake and Service (2021) and InSight Marsquake and Service (2022). The global seismic event rate sets Mars as moderately active, between the weak lunar activity and the terrestrial intraplate seismicity (Banerdt et al, 2020). However, no marsquakes of magnitude greater than four have been reported in MQS v9 and only a fraction of events exhibit clear body waves arrivals. In addition, none of the events show surface waves of amplitude greater than the Martian noise (Giardini et al, 2020), and depth phases pP and sS are difficult to identify in the data, making it complicated to estimate the hypocenter depths.

Despite their low magnitude, the ten largest recorded low frequency

* Corresponding author.
E-mail address: alice.jacob.gm@gmail.com (A. Jacob).

https://doi.org/10.1016/j.tecto.2022.229434
Received 17 December 2021; Received in revised form 24 May 2022; Accepted 28 May 2022
Available online 6 June 2022
0040-1951/© 2022 The Authors. Published by Elsevier B.V. This is an open access article under the CC BY license (http://creativecommons.org/licenses/by/4.0/).

events have been used for determining the first internal structure models of Mars from the crust to the core (Lognonné et al, 2020; Khan et al, 2021; Knapmeyer-Endrun et al, 2021; Stähler et al, 2021). More specifically, based on the receiver functions study of Lognonné et al (2020) and confirmed in Knapmeyer-Endrun et al (2021), the first ten kilometers of the upper crust beneath the InSight landing site appear highly altered and fractured. Below this first crustal discontinuity, as proposed by the seismic reflected phases analysis of Knapmeyer-Endrun et al (2021), two models are described with two and three layers. For both velocity models, the martian equivalent of Moho discontinuity is located at 20 ± 5 km depth, and an additional discontinuity at 39 ± 8 km depth is estimated in the case of the three layers model. On a more regional scale, the upper mantle has been constrained with the first clear identifications of secondary phases, PP, PPP, SS and SSS (Khan et al, 2021) which confirmed an upper mantle structure controlled by a thermal lithosphere with a 400–500 km thickness. Finally, the observation of ScS core phases (Stähler et al, 2021) provided the first seismic estimation of the core radius at 1830 ± 40 km.

On the source aspects and after the first magnitude estimations of Giardini et al (2020) and InSight Marsquake and Service (2021), Brinkman et al. (2021) have performed the first Martian moment tensors inversion for the two largest events, S0173a and S0235b. They not only highlighted the fact that single station methodology is sufficient to obtain stable and interpretable focal mechanism solutions but got also results in strong agreement with orbital imagery observations of an extensive regime and the global azimuths of Cerberus fossae. They also demonstrate the robustness of an inversion exclusively based on body waves despite strong assumptions on the internal model.

With an additional year of monitoring, we can now add seven additional LF and BB events to continue this single station source inversion. Even if less powerful than S0173a and S0235b, these new events are characterized by clear arrivals of P and S waves, high signal-to-noise ratio (SNR) and magnitude M_w larger than 3 (InSight Marsquake and Service, 2021 and see Table 1 for details). They have been located between 25 and 40 to the east of InSight (*i.e.* corresponding to distances of 1500–2500 km) with 3 to 4 error ellipsoids (from MQS catalog, InSight Marsquake and Service, 2021, and based on Drilleau et al, 2022 estimations). Five of them, like S0173a and S0235b, are located in the vicinity of the Cerberus fossae faults (Fig. 1) and confirm its seismicity. Cerberus fossae is a major graben system (*e.g.* Vetterlein and Roberts, 2010; Roberts et al, 2012) and one of the largest structures close to the InSight landing site. Before the InSight mission, it was already studied with remote sensing data (Knapmeyer et al., 2006; Roberts et al., 2012; Taylor et al., 2013) and was already referred as a potential seismic source with an average annual seismic moment release of 10^{15}-10^{17} Nm/yr (Taylor et al, 2013; Perrin et al, 2022). In addition, recent volcanic activity is inferred in the region of Elysium Planitia (Vaucher et al, 2009; Hauber et al, 2011) and potentially associated with the regional seismic activity. The remaining event S0784a is located further south, and event S0325a is located on the Martian dichotomy that separates the contrasting terrains of the north and south and characterized by crustal structural complexities.

The main motivation of our study is that these marsquakes exhibit specific characteristics typical of tectonic earthquakes and located near peculiar volcanic/tectonic features. Consequently, here we propose a seismo-tectonic analysis of the region to the east of InSight by constraining the seismic moment tensor of the nine seismic events aforementioned. The moment tensor is a good geometrical representation of the seismic source and is classically used to describe the faulting motion at the origin of quakes (*e.g.,* Molnar and Sykes, 1969; Michael, 1987; Henry et al, 2002). With InSight we are fortunate to be able to process the first seismic data on Mars, although restricted by the fact that there is currently only one seismic station on the ground surface. On the contrary, on Earth, seismic signals are usually recorded from dozen to hundreds of stations. The Earth data are moreover very well located geographically and at depth, compared to Martian data. Earth-based moment tensor analyses from a single station are only preliminary or exceptional works and from signals with a fairly larger SNR. Moreover, the internal structure is much better constrained for the Earth with high resolution 3D velocity models built from multiple decades of data accumulation.

After Brinkman et al. (2021), the seven additional events will allow us to explore more deeply the seismo-tectonic context of Elysium Planitia. For that matter, we invert the moment tensors and discuss the results in terms of seismic origins, linked with the morphological observations of the region. Our methodology is principally based on a grid-search exploration over the three double-couple angles, *i.e.* the strike, the dip and the rake. For that matter, we invert P and S waveforms while estimating the seismic moment and the seismic attenuation. We also invert and compare the amplitudes of the secondary phases PP, SS, PPP and SSS following their identification by Khan et al (2021) and Drilleau et al (2022). In addition, we provide estimates for the hypocenter depths and we then discuss why the absence of surface wave observations in the SEIS records do not exclude a crustal origin.

The paper is organized as follows: in Section 2 we first describe the general geological context and in Section 3 we present the InSight seismic data. In Section 4 we explain the inversion method. Then, the detailed results for S0235b and the general results of the nine marsquakes are presented in Section 5. Finally, in Section 6 we discuss the potential seismic sources, by comparing the selected mechanisms with the nearby major structures.

2. Regional context

InSight has landed in Elysium Planitia at 4 . 5N 1356E, south of the Elysium Mons volcanic structure and near the dichotomy boundary (Fig. 1). From crater counting and geological unit series, the landing site is characterized by geological structures aged from Hesperian (3.7 to 3.2 Ga ago) to Early Amazonian (3.2 Ga to few ka ago, Tanaka et al, 1992; Warner et al, 2017; Golombek et al, 2018, 2020). The marsquakes

Table 1
Source parameters of the considered events. The table summarizes the quality (A or B) and the type of the event data (Low-frequency LF or Broadband BB), the magnitude (M_w, with errors), the epicentral distance (Δ, with their errors), the back-azimuth (BAZ, with errors), the quake origin time (stated in UTC time, in the Earth reference frame, as YYYY-MM-DDThh:mm:ss) and the frequency bandwidth for the bandpass filter applied to both the data and the synthetics. [(1)] Values from V7 MQS catalog (InSight Marsquake and Service, 2021); [(2)] Locations from Drilleau et al (2022). The selected Δ and BAZ are in bold.

	Quality, type	$M_w^{(1)}$	$\Delta^{(1)}$ (°)	$\Delta^{(2)}$ (°)	$BAZ^{(1)}$(°)	$BAZ^{(2)}$ (°)	Origin time (UTC)	Frequency range (Hz)
S0173a[(1)]	A, LF	3.7 (±0.3)	**29.3 (±1.8)**	29.8 (±2.0)	**91 (±12)**	88 (±16)	2019-05-23T02:19:16	0.14-0.4
S0235b[(1)]	A, BB	3.6 (±0.2)	**27.9 (±1.6)**	29.3 (±2.2)	**74 (±12)**	69 (±18)	2019-07-26T12:15:45	0.14-0.5
S0325a[(2)]	B, LF	3.7 (±0.3)	38.5 (±6.0)	**40.8 (±3.2)**	-	**125 (±17)**	2019-10-26T06:58:55	0.14-0.4
S0407a[(2)]	B, LF	3.0 (±0.2)	28.6 (±2.2)	**27.9 (±2.1)**	-	**79 (±25)**	2020-01-19T09:54:08	0.14-0.5
S0409d[(2)]	B, LF	3.2 (±0.2)	30.4 (± 5.9)	**29.6 (± 2.5)**	-	**82 (± 25)**	2020-01-21T11:30:42	0.14-0.5
S0484b[(2)]	B, BB	2.9 (±0.2)	30.9 (± 6)	**30.4 (± 2.3)**	-	**73 (± 34)**	2020-04-07T08:48:32	0.14-0.4
S0784a[(2)]	B, BB	3.3 (±0.2)	33.4 (± 3.6)	**28.6 (± 3.4)**	-	**101 (± 17)**	2021-02-09T12:11:37	0.14-0.4
S0809a[(3)]	A, LF	3.3 (±0.2)	**28.9 (± 2.0)**	29.7 (± 2.7)	**87 (± 20)**	86 (± 15)	2021-03-07T11:09:33	0.14-0.5
S0820a[(3)]	A, LF	3.3 (±0.2)	**29.3 (± 2.4)**	28.7 (± 3.9)	**88 (± 19)**	84 (± 18)	2021-03-18T14:51:27	0.14-0.5

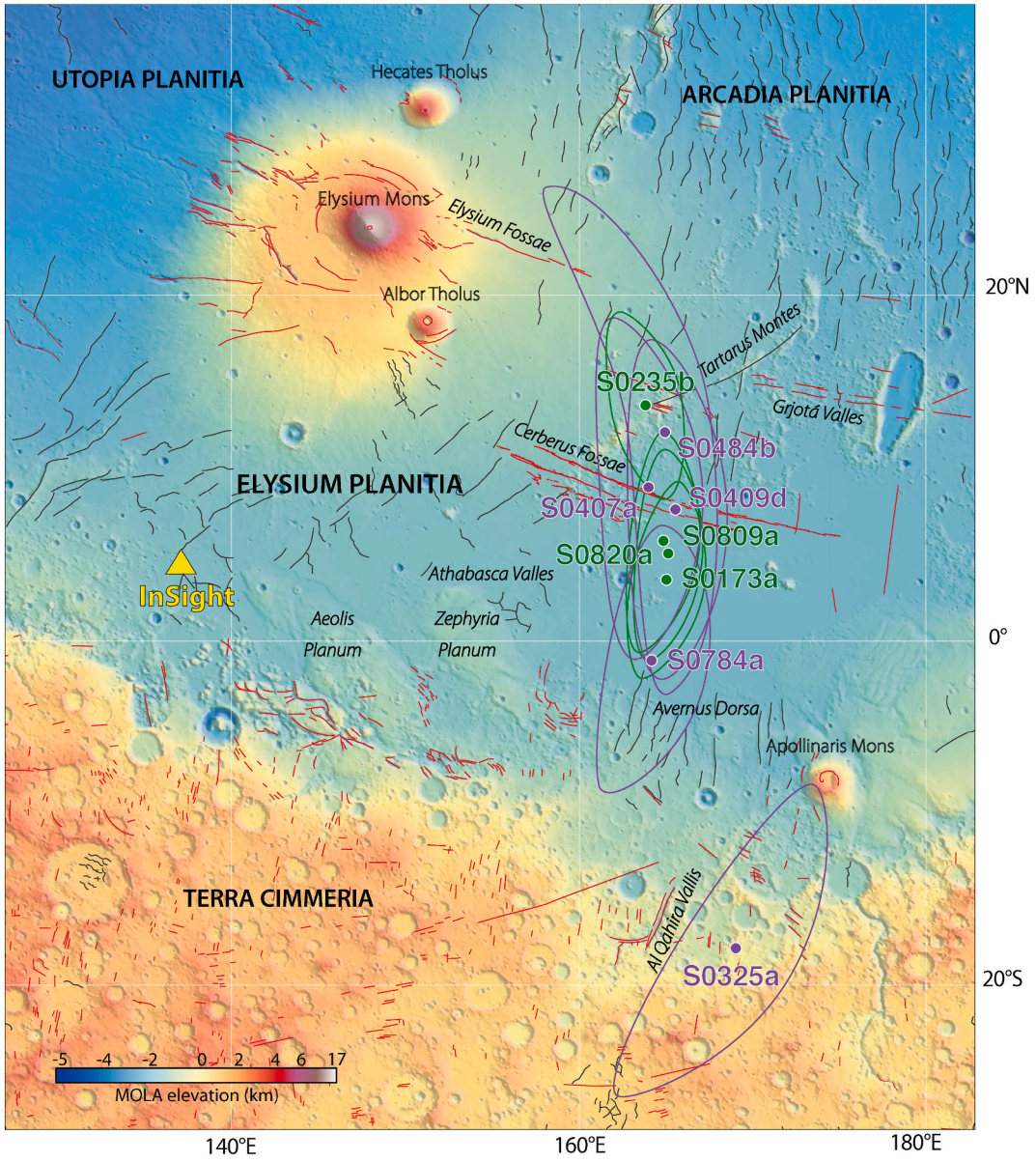


Fig. 1. Topographic map (MOLA elevation) of the region to the east of InSight with the main tectonic structures and locations of the studied marsquakes. InSight landing site is represented with a yellow triangle, the compression structures are highlighted in black lines and the extensive structures are in red (compiled by Knapmeyer et al., 2006). Cerberus fossae fault system is mapped with a thicker red line (Perrin et al, 2022). The quality A event ellipsoids of the MQS catalog are displayed in light green (InSight Marsquake and Service, 2021), and the quality B event ellipsoids of Drilleau et al (2022) are circled in purple. (For interpretation of the references to color in this figure legend, the reader is referred to the web version of this article.)

S0173a, S0235b, S0407a, S0409d, S0484b, S0809a and S0820a are centered on the Cerberus fossae system while S0784a is located on lava plains in the southern vicinity of InSight and S0325a is located at the dichotomy boundary. Marsquakes S0173a, S0235b, S0809a and S0820a ellipsoids are determined by the InSight MQS InSight Marsquake and Service (2021) (green ellipsoids on Fig. 1) and the events S0325a, S0407a, S0409d, S0484b and S0784a are located by Drilleau et al (2022) (purple ellipsoids on Fig. 1). The location errors are large, ranging from ± 3 (about ±200 km) to ± 5 (about ±300 km) depending on the data quality. The ellipsoids can therefore cut across several regions over several hundreds of kilometers (*e.g.* in the case of S0484b which extends from Elysium Mons to the south of the Cerberus fossae system).

The center part of our study area is located on the Elysium Planitia terrains, expanding from the high plateaus of Aeolis and Zephyria, crossing the channels of Athabasca Valles and the graben systems of Cerberus fossae and Grjotá Valles (thick red lines on Fig. 1). Elysium Planitia, and more generally Mars, demonstrates many evidences of simultaneous or contemporaneous ages of hydrological and volcanic processes, notably with the observations of surficial guiding channels filled with lava flows (Berman and Hartmann, 2002; Burr et al, 2002; Plescia, 2003; Jaeger et al, 2007). The youngest lava flows are dated from 300 Ma to 20 Ma based on crater dating studies (Berman and Hartmann, 2002; Vaucher et al, 2009; Hauber et al, 2011) and originated from recent volcanic activity in the central plains of Elysium Planitia form the Cerberus fossae volcanic unit. The fissures of Cerberus fossae would have enabled the flow of large volumes of these lavas as recently as 2.5 Ma ago (Vaucher et al, 2009; Golder et al, 2020), and then escaping towards Athabasca Valles (Burr et al, 2002; Plescia, 2003; Vaucher et al, 2009). It has been also suggested that other channels surrounding Grjotá Valles have been formed by catastrophic overflows (Berman and Hartmann, 2002; Burr et al, 2002; Plescia, 2003). The large

amounts of lava that have rapidly emerged from these channels have led to the hypothesis that massive dike networks exist in the subsurface (Ernst et al, 2001). These inferences would be in favor of a rather recent and dominant volcanic activity. Besides, magma transport and the potential magmatic chamber pressurization are known to generate seismicity on Earth (Grandin et al, 2012; Carrier et al, 2015).

Cerberus fossae (red thick lines in Fig. 1) is described by Perrin et al (2022), Taylor et al (2013) and Vetterlein and Roberts (2010) as a possible large dike-induced graben system of ~1200 km long located at 1500 km in the north-east of the InSight lander and in the northern part of Elysium Planitia. The orientation of the fossae (N100-110E) is coherent with the geometry of the supposed underlying dikes radiating away from Elysium Mons (Ernst et al, 2001). In addition, the Elysium Mons volcanic edifice is at the origin of a regional loading of the lithosphere with a negative Bouguer gravity anomaly (Neumann et al, 2004; Belleguic et al, 2005; Baratoux et al, 2014, and see Supplementary material S12), and may has experienced several and continuous episodes of activity between 4 and 2 Ga ago (Platz and Michael, 2011; Pasckert et al, 2012; Pan et al, 2020). The deformation associated with this regional loading may have impacted the formation of Cerberus fossae. Besides, Perrin et al (2022) observed that the widths and throws along the fossae decreased eastward, suggesting long-term propagation of the deformation away from Elysium Mons. This also implies that seismic activity is possible in the eastern, younger and less evolved parts of Cerberus fossae. Taylor et al (2013) have furthermore proposed that the recent tectonics activity of Cerberus fossae is less than 10 Myr, and they described the faults as active seismic sources with a general estimated seismic moment release of 10^{15}-10^{17} Nm/yr. This last value is larger than the observed Martian seismicity by about two orders of magnitude (Giardini et al, 2020). However, the seismic data recorded by InSight are consistent with the estimate by Taylor et al (2013) of 1.5 to 1.9 x 10^5 events generated per year from Cerberus fossae and furthermore, correspond to the present seismicity of Cerberus, while the one estimated from remote sensing is averaged since the onset of Cerberus activity. These two estimations can therefore be more coherent if one assume a time decrease of the seismicity of Cerberus. A dozen of events have indeed been detected and located in the vicinity of the graben system (Drilleau et al, 2022; InSight Marsquake and Service, 2022 and Fig. 1), although their exact seismic origin is not firmly established (see Section 6).

The southern end of the study area (red-yellow cratered terrains in Fig. 1) encompasses the Martian dichotomy in the Terra Cimmeria lands including the Apollinaris volcano and the ancient flood valley of Al Qahira Vallis. The dichotomy is a giant planetary structure located around the planet's equator and separating the oldest cratered highlands in the south aged about 4 Ga (Tanaka et al, 2011), from the younger lowlands in the north dated between 3 Ga and several ka ago (Tanaka et al, 2011). The highlands and the lowlands have a ground elevation difference of 4 to 6 km. The dichotomy boundary has formed very early and has been subjected to many sedimentary accumulations and morphological reworking in a large part of the history of Mars (Frey et al, 2002). These successive sedimentary and volcanic processes have led to the formation of complex structures in the shallow crust of Mars including the upper regolith (Tanaka et al, 2011; Golombek et al, 2018; Pan et al, 2020). These complexities, as well as the very pronounced relative elevation contrast between the two hemispheres, are suspected to destabilize the seismic propagation notably by adding reverberation or crustal diffraction (Tauzin et al, 2019; Lognonné et al, 2020; Knapmeyer-Endrun et al, 2021).

3. Seismic data from SEIS/InSight

3.1. Data generalities: frequency content and quality

The InSight seismic events are named according to the Martian sol (the Martian day since the beginning of the mission) on which they occurred and numbered in alphabetical order, *e.g.,* S0235b occurred on 235*th* sol, after S0235a.

First, the seismic event classification is done according to the frequency band in which the marsquakes have the most energy (for a complete overview of the seismic events classification, see Clinton et al, 2021). Thus, two main families are identified, the family of low-frequency events where the energy is observed mostly below 2.4 Hz, and the high-frequency events family with energy mostly above 2.4 Hz.

The family of low-frequency events contains the LF events (low-frequency), whose main energy lies below 2.4 Hz, and the BB events (broadband) events, with their main energy below 2.4 Hz but with a possible excitation above 2.4 Hz. The LF and BB events are quite similar to each other. Their signals are characterized by an overall duration generally of 10 to 20 minutes with two distinct *P* and *S* phases, where the *S*-wave is more amplified than the *P*-wave. The SNR of these events is the highest among the entire seismic events catalog, on average from 2.5 to 20, and up to a factor of 200 (Banerdt et al, 2020; Giardini et al, 2020; InSight Marsquake and Service, 2022). Besides, spectrum analyses of LF and BB events have shown that they are similar to teleseismic earthquakes and shallow moonquakes (Banerdt et al, 2020; Giardini et al, 2020). Brinkman et al. (2021) further concluded on a probable tectonic origin with little diffraction for three LF/BB events (*i.e.*, S0173a, S0235b and S0183a) and suggested that S0235b and S0173a share a common origin. The low-frequency family is thus constituted by tectonic events, and we focus exclusively on their seismo-tectonic analysis in this manuscript.

The second family, the high-frequency events, includes the 2.4 Hz, the HF (high-frequency), the VF (very high-frequency) and the SF (super high-frequency) events (see van Driel et al, 2021 for a complete description of the high-frequency family). The 2.4 Hz events are excited around 2.4 Hz with a very limited excitation above or below. HF events are centered on 2.4 Hz and above mainly. A special case of HF, the VF, are characterized by a significantly larger energy on the horizontal components than on the vertical component at high frequencies. Finally, a last class identified are the SF seismic events with energy at more than 5 Hz and up to 50 Hz. The HF, VF and 2.4 Hz are not located, so their analysis is based exclusively on the interpretation of their spectrum, and they are suggested to be small and shallow marsquakes (Clinton et al, 2021; van Driel et al, 2021). The SF are supposed to be related to local thermal variations (Dahmen et al, 2021).

In addition, all of the recorded marsquakes are classified with a quality grade from A to D (Clinton et al, 2021). From MQS definitions, quality A quakes correspond to high SNR events with clearly identified phases as well as the polarization of the *P*-wave and the *S*-wave trains, which provides the back-azimuth (BAZ) of the epicenter. Quality B events are very similar to quality A in terms of phases identification and waveforms, but without clear polarization and therefore less precise BAZ. For the C quality data, phases are observed but, either they are not identified, or only a single phase is identified, or multiple phases are identifiable but no clear *P* and *S*-waves can be attributed to them. The D quality events are the lowest quality data and are characterized by weak signals, or are likely not attributable to a seismic event (suspicious data). Since 2019, InSight has recorded a majority of high frequency events family, with more than 700 2.4 Hz events, more than 1000 SF, 95 HF and 56 VF, whereas only 44 LF and 25 BB events have been recorded to date (InSight Marsquake and Service, 2022). 6 events are of quality A (LF/BB events exclusively), 133 are of quality B, more than 500 are of quality C and more than 800 are of quality D.

The InSight seismic data (InSight Mars SEIS Data Service, 2019) contain large amounts of glitches, described as a transient instrumental noise likely associated to thermal tilts or dislocations (Lognonné et al, 2020; Scholz et al, 2020). In practice, glitches are characterized by a high amplitude pulse of generally 10^{-8} m/s. Two of our selected LF events, S0173a and S0409d, are contaminated on the *P*-wave by glitches. Fortunately, S0173a glitch arrives long enough after the main *P*-wave peak and does not affect our calculations, while we use the

deglitched S0409d time series (with the IPGP deglitching technique, Scholz et al, 2020).

In this study, we select nine marsquakes exclusively in LF/BB frequency ranges and of qualities A and B. They all display clear picks of *P*- and *S*-waves, high SNR, and have been located with small error bars (see Section 3.2 below).

3.2. Seismic event locations and depths

Events S0173a, S0235b, S0809a and S0820a have been located by MQS (InSight Marsquake and Service, 2021; Giardini et al, 2020). These locations are shown by the green probability ellipsoids on Fig. 1. The BAZ was calculated from polarization analysis of the first *P*-waveform and the epicentral distance was deduced from the *P–S* time delay and pre-launch *a priori* velocity models (Khan et al, 2016; Böse et al, 2017; Clinton et al, 2017).

The recent work from Drilleau et al (2022) proposes additional BAZ values for other qualities A and B events. This is measured with the energy along the horizontal component, in addition to correlation and coherency coefficients between horizontal and vertical components. These BAZ estimations and epicentral distances are moreover in good agreement with MQS ones for the quality A events, and allow to add news locations for 5 quality B events (S0325a, S0407a, S0409d, S0484b and S0784a). Their locations are represented by the purple ellipsoids on Fig. 1. The epicentral distance, BAZ and origin time of all events are listed in Table 1.

The depths of the events are not precisely known, but the values are in agreement for seismic sources at moderate depths below the Moho (~ 30 km with large errors) for most of the LF/BB events (Brinkman et al., 2021; Drilleau et al, 2022). However, the observed pP and sS depth phases (Brinkman et al., 2021, Drilleau et al, 2022 and Stähler et al, 2021) provide depth constraints with uncertainties of several tens of kilometers. Last but not least, the lack of clear observations of surface waves in the InSight data does not seem to support shallow seismic sources. This raises concerns about the nature of the source and the link with shallow and/or crustal tectono-volcanic activity, and will be addressed later in Section 6.

4. Moment tensor inversion methodology

With only one seismic station and the uncertainties on Mars structure and a strong observed scattering (Lognonné et al, 2020; Karakostas et al, 2021; Menina et al, 2021; van Driel et al, 2021) we had to adapt the classical moment tensor inversion method used on terrestrial data. Our approach is based on a grid-search exploration method for which we are seeking three source parameters: strike, dip and rake angles. Therefore, this inversion resolves the double-couple (DC) solutions of the moment tensors and will restrict the analyses to fractures or faulting sources. The isotropic (ISO) and compensated linear vector dipole (CLVD) components of the moment tensor will therefore be ignored, which might be a limiting factor for tremor sources in Cerberus fossae (Kedar et al., 2021). The DC components represent the fault direction (strike), steepness (dip), and movement (rake) and are visualized in a spherical space through focal mechanisms (Jost and Herrmann, 1989; Henry et al, 2002). In addition, the solutions are non-unique following two conjugate fault planes (or nodal planes), which correspond to the two triplets of strike, dip and rake angles.

For each parameters combination, we compute a cost function composed by several fitting terms with weighting factors. Those with the lowest cost function correspond to the best-predicted moment tensor solutions. The methodology differences with Brinkman et al. (2021) are the following:

- in order to improve the waveform fitting, we also explore the apparent attenuation of the direct phases through an apparent quality factor *Q*. As compared to previous estimations which inverted *Q* and the seismic moment through displacement spectral fitting (Giardini et al, 2020), the *Q* factor and the seismic moment M_0 are inverted in the time domain for ground velocity, taking advantage that the InSight noise has been found flat in ground velocity in the bandwidth of interest (Lognonné et al, 2020; Stutzmann et al., 2021) and can therefore be considered as white. This is likely reducing the impact of long period noise in the inversion.
- In addition to the body waveform fitting, we add the fitting of the secondary phase amplitudes of PP, SS, PPP and SSS as supplementary constrains.
- Last but not least, we account for the non-observation of surface waves and reject solutions with synthetic surface wave amplitudes larger than recorded amplitudes in the data surface wave windows.

4.1. Synthetic seismograms computation

We use the Direct Solution Method (DSM) Kernel Suite (Geller and Ohminato, 1994; Geller and Takeuchi, 1995; Fuji et al, 2012, 2016) for an efficient Green's functions computations, this being done for the six components of DC source and all distances between source and stations.

In our case, DSM is computing synthetics for a spherically symmetric Mars model with discontinuities. We use the "TAYAK" model (Khan et al, 2016), which integrated the pre-launch knowledge on Mars (Smrekar et al, 2019), but modified it to account for the crustal structure, as constrained by the receiver functions analysis of Lognonné et al (2020) and Knapmeyer-Endrun et al (2021).

This updated TAYAK model is displayed on Fig. 2. The crust includes therefore a first interface at 10 km (Lognonné et al, 2020) and has the crust-mantle discontinuity at 24 km (Knapmeyer-Endrun et al, 2021), which we will simplify with the term "Moho" hereafter. Another modified TAYAK model with a 3*rd* discontinuity boundary at 43 km depth (potentially the Moho discontinuity) as proposed by Knapmeyer-Endrun et al (2021), has also been used for sensitivity tests in Supplementary material S11. Our inversion methodology does not invert the arrival times of the direct phases nor those of the secondary phases but explore differences in attenuation. We are therefore mostly sensitive to the differences in the elastic geometrical spreading with respect to other models, including those recently proposed by Khan et al (2021) and Stähler et al (2021). These differences are integrated in the final determination of the seismic moment, but not in the geometry of the source.

The DSM Green's functions are pre-calculated up to 0.8 Hz (or period of 1.25 sec) at the fixed epicentral distances and BAZs compiled on Table 1. The synthetics cover therefore the bandwidth used for inversion, which is generally 0.1–0.5 Hz. They are computed with source depths up to 90 km, which includes widely the depth ranges proposed by Brinkman et al. (2021), Drilleau et al (2022) or Khan et al (2021).

The synthetics are computed with a very low attenuation, *i.e.* a large initial quality factor Q_0 of 2000 and the phase attenuation is therefore modeled in the phase inversion process.

4.2. Time series pre-processing and inversion setup

We pre-process the 20 sps (sample per second) SEIS VBB raw data by detrending and removing the instrumental response, from counts to ground velocity. A high pass filter with a cutoff frequency of 0.006 Hz was used in the instrument correction.

The three axis VBB data, as recorded on the sensor directions U,V,W, are then rotated to vertical-radial-transverse (ZRT) components based

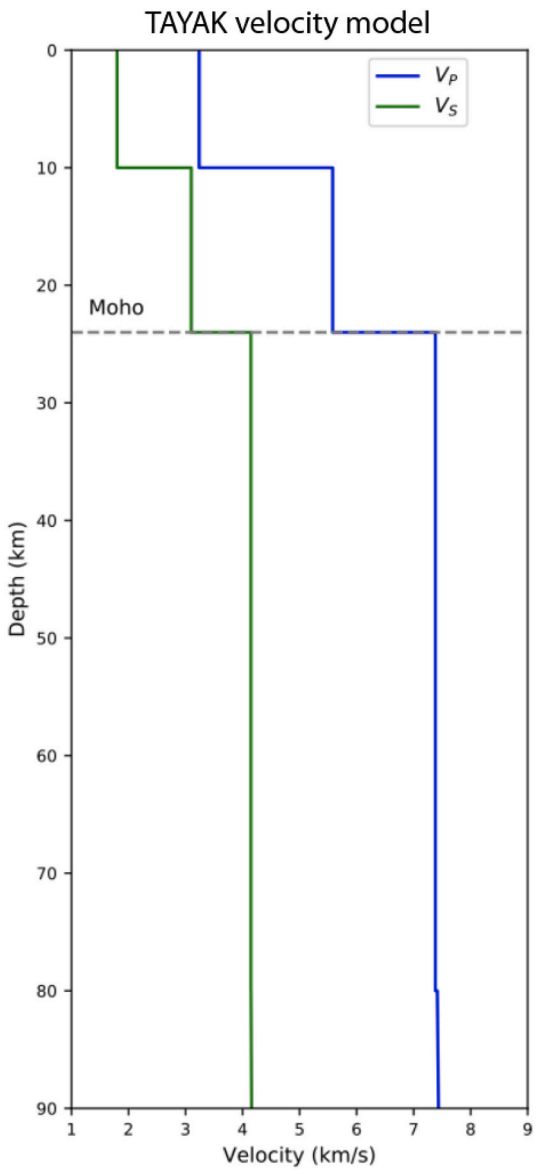


Fig. 2. TAYAK velocity model used in the synthetic seismograms computation. The velocity model includes the upper crustal model based on Lognonné et al (2020) and the deeper crustal information on the equivalent Martian Moho depth from Knapmeyer-Endrun et al (2021). V_P and V_S are displayed in blue and green, respectively. (For interpretation of the references to color in this figure legend, the reader is referred to the web version of this article.)

on the event BAZs (InSight Marsquake and Service, 2021; Drilleau et al, 2022). The same is made for the synthetics from ZNE to ZRT. Then, the time series are band pass filtered, in bandwidths depending on the energy content of each event (the considered parameters are listed on Table 1).

4.3. Moment tensor grid search: generation of synthetics

The first grid-search exploration is conducted in the depth range of 12 – 90 km with a 3 km step. For each depth, we explore all moment tensor geometries with strike, dip and rake respectively between 0 and 360, with a 9 step, between 0 and 90, with a 4 step and between −180 and 180, with a 9 step. Then strike, dip and rake are converted into the full moment tensor components M_{rr}, $M_{\theta\theta}$, $M_{\phi\phi}$, $M_{r\theta}$, $M_{r\phi}$ and $M_{\theta\phi}$ where r, θ and ϕ correspond to spherical coordinates in the up-south-east convention. The six corresponding synthetic Green's function are then multiplied by these components and summed up to generate the synthetic corresponding to an unitary moment tensor (MT).

4.3.1. P and S waveform fits: quality factor, seismic moment and phase shift

Due to the uncertainties on the velocity model and in order to adjust the amplitude of the synthetics to the data, we perform a secondary grid-search over the seismic attenuation $1/Q$ and phase shift and invert linearly the associated seismic moment M_0.

The seismic attenuation integrates both the intrinsic (Q_i) and scattering (Q_c) and is generally approximated as $1/Q = 1/Q_i + 1/Q_c$ (Romanowicz and Mitchell, 2015). It is far to be at this time constrained for Mars, and proposed values for Q_S are of the order of 300–500 for lithospheric path (Brinkman et al., 2021; Giardini et al., 2020). On the long period side of the LF-BB events (0.1–0.5 Hz), assuming a predominance of intrinsic attenuation mostly related to shear is a reasonable approximation, which leads to $Q_P \propto 9/4 \cdot Q_S$. On the shorter period side (0.5–2.5 Hz), scattering is likely dominating, with not only smaller Q_S but with also smaller Q_P/Q_S and therefore a subsequent complexity on the *a priori* Q_P/Q_S ratio as well as frequency dependency (see Aki, 1997 for an overview of the impacts of scattering on the quality factor). Based on the uncertainties on the Q_P/Q_S ratio for short period waves, we therefore limit our analysis to the long period side and keep the $Q_P \propto 9/4 \cdot Q_S$ ratio.

Thus, we invert the quality factor in a waveform fitting process. For that, we explore both new quality factors Q_P for *P*-wave on the Z (PZ) and R (PR) components, and Q_S for *S*-wave on the Z (SZ) and T (ST) components. Exploration is made for Q_S ranging from 160 and 670 with step of 25 (equivalent to Q_P ranging from 360 to 1500, with step of 57). It includes the effective $Q \sim 300$ proposed by Giardini et al (2020) for LF events at distances ranging from 25 to 45° as well as Mars *a priori* Q_μ (Smrekar et al, 2018; Lognonné and Mosser, 1993).

To perform the attenuation correction, the spectra of the synthetic body wave timeseries are calculated over a window starting on the arrival times computed by the TauP toolkit (Crotwell et al, 1999) and with a duration of ±20 seconds around the phase in order to minimize Gibbs effects. The original synthetic spectrum $S_0(\omega)$ is thus corrected with a ω^2 source (Aki, 1980) and attenuation terms as:

$$S(\omega) = \frac{S_0(\omega)}{1 + \left(\frac{\omega}{\omega_c}\right)^2} \cdot \exp^{-\frac{\omega T}{2}\left(\frac{1}{Q} - \frac{1}{Q_0}\right)}, \tag{1}$$

where ω and ω_c are the angular frequency and cutoff frequency respectively, and T is the wave propagation time. The cutoff frequencies, different for P and S, are following the scaling laws of Sato and Hirasawa (1973), similar to those used by Mocquet (1999):

$$\begin{aligned} log_{10}\left(\frac{\omega_c^P}{2\pi}\right) &= 5 - 0.35 \cdot log_{10}(M_0), \\ log_{10}\left(\frac{\omega_c^S}{2\pi}\right) &= log_{10}\left(\frac{\omega_c^P}{2\pi}\right) - 0.2. \end{aligned} \tag{2}$$

The M_0 stands for the MQS estimations for all the marsquakes as a first step (see Table 1).

Then, once the new attenuated spectra S is calculated from Eq. (1), for each $Q_P - Q_S$, we explore the seismic moment M_0 and the phase shift. We determine the phase shift between the synthetic and the observed signal computed on a window of ± 1.5 seconds centered on the

maximum of the observed body wave. Thus, we allow the phase exploration over one wavelength around the maximum of amplitude. We define τ_p and τ_s as the delays on the *P*- and the *S*-waves respectively.

We invert the body waveforms by computing the following variance function η between synthetics and observed data on the 4 components:

$$\begin{aligned}\eta &= \int_{\Delta T_p} \mathrm{dt}\left[\varepsilon^{\mathrm{PZ}}\left[\mathrm{d}^{\mathrm{PZ}}_{\mathrm{obs}}(t) - M_0\ \mathrm{d}^{\mathrm{PZ}}_{\mathrm{syn},\mathrm{Q_P}}(t-\tau_p)\right]^2 + \varepsilon^{\mathrm{PR}}\left[\mathrm{d}^{\mathrm{PR}}_{\mathrm{obs}}(t) - M_0\ \mathrm{d}^{\mathrm{PR}}_{\mathrm{syn},\mathrm{Q_P}}(t-\tau_p)\right]^2\right] \\ &+ \int_{\Delta T_s} \mathrm{dt}\left[\varepsilon^{\mathrm{SZ}}\left[\mathrm{d}^{\mathrm{SZ}}_{\mathrm{obs}}(t) - M_0\ \mathrm{d}^{\mathrm{SZ}}_{\mathrm{syn},\mathrm{Q_Z}}(t-\tau_s)\right]^2 + \varepsilon^{\mathrm{ST}}\left[\mathrm{d}^{\mathrm{ST}}_{\mathrm{obs}}(t) - M_0\ \mathrm{d}^{\mathrm{ST}}_{\mathrm{syn},\mathrm{Q_Z}}(t-\tau_s)\right]^2\right]\end{aligned} \tag{3}$$

where $d^C_{\mathrm{syn},Q}$ is the inverse Fourier transform of *S* for the direction C (Eq. (1)) and d^C_{obs} is the observed time series along the same direction (C being Z,R or T for either *P* or *S*-wave) and ΔT_p and ΔT_s are the time window of the inverted body waves.

η is rewritten in a vector-way as:

$$\begin{aligned}\eta &= \varepsilon^{\mathrm{PZ}}\left[\mathrm{d}^{\mathrm{PZ}}_{\mathrm{obs}} - M_0\ \mathrm{d}^{\mathrm{PZ}}_{\mathrm{syn},\mathrm{Q_P},\tau_\mathrm{p}}\right]^2 + \varepsilon^{\mathrm{PR}}\left[\mathrm{d}^{\mathrm{PR}}_{\mathrm{obs}} - M_0\ \mathrm{d}^{\mathrm{PR}}_{\mathrm{syn},\mathrm{Q_P},\tau_\mathrm{p}}\right]^2 \\ &+ \varepsilon^{\mathrm{SZ}}\left[\mathrm{d}^{\mathrm{SZ}}_{\mathrm{obs}} - M_0\ \mathrm{d}^{\mathrm{SZ}}_{\mathrm{syn},\mathrm{Q_Z},\tau_\mathrm{s}}\right]^2 + \varepsilon^{\mathrm{ST}}\left[\mathrm{d}^{\mathrm{ST}}_{\mathrm{obs}} - M_0\ \mathrm{d}^{\mathrm{ST}}_{\mathrm{syn},\mathrm{Q_Z},\tau_\mathrm{s}}\right]^2,\end{aligned} \tag{4}$$

where **d** are the vectors of all samples of $d(t)$ in the time window.

The seismic moment M_0 is computed for each set of parameters (*i.e.* MT geometry, Q_P, Q_S, τ_p, τ_s) obtained by solving the linear inverse problem $M_0 = \frac{A}{B}$, where:

$$\begin{aligned}A &= \varepsilon^{\mathrm{PZ}} \times \mathrm{d}^{\mathrm{PZ}}_{\mathrm{obs}}.\mathrm{d}^{\mathrm{PZ}}_{\mathrm{syn},\mathrm{Q_P},\tau_\mathrm{p}} + \varepsilon^{\mathrm{PR}} \times \mathrm{d}^{\mathrm{PR}}_{\mathrm{obs}}.\mathrm{d}^{\mathrm{PR}}_{\mathrm{syn},\mathrm{Q_P},\tau_\mathrm{p}} \\ &+ \varepsilon^{\mathrm{SZ}}\mathrm{d}^{\mathrm{SZ}}_{\mathrm{obs}}.\mathrm{d}^{\mathrm{SZ}}_{\mathrm{syn},\mathrm{Q_S},\tau_\mathrm{s}} + \varepsilon^{\mathrm{ST}}\mathrm{d}^{\mathrm{ST}}_{\mathrm{obs}}(t).\ \mathrm{d}^{\mathrm{ST}}_{\mathrm{syn},\mathrm{Q_S},\tau_\mathrm{s}} \\ B &= \varepsilon^{\mathrm{PZ}} \times \mathrm{d}^{\mathrm{PZ}}_{\mathrm{syn},\mathrm{Q_P},\tau_\mathrm{p}}.\mathrm{d}^{\mathrm{PZ}}_{\mathrm{syn},\mathrm{Q_P},\tau_\mathrm{p}} + \varepsilon^{\mathrm{PR}} \times \mathrm{d}^{\mathrm{PR}}_{\mathrm{syn},\mathrm{Q_P},\tau_\mathrm{p}}.\mathrm{d}^{\mathrm{PR}}_{\mathrm{syn},\mathrm{Q_P},\tau_\mathrm{p}} \\ &+ \varepsilon^{\mathrm{SZ}}\mathrm{d}^{\mathrm{SZ}}_{\mathrm{syn},\mathrm{Q_S},\tau_\mathrm{s}}.\mathrm{d}^{\mathrm{SZ}}_{\mathrm{syn},\mathrm{Q_S},\tau_\mathrm{s}} + \varepsilon^{\mathrm{ST}}\mathrm{d}^{\mathrm{ST}}_{\mathrm{syn},\mathrm{Q_S},\tau_\mathrm{s}}.\ \mathrm{d}^{\mathrm{ST}}_{\mathrm{syn},\mathrm{Q_S},\tau_\mathrm{s}}.\end{aligned} \tag{5}$$

We deduce the best set of $Q_P - Q_S - M_0 - \tau_p - \tau_s$ from the lowest η function, which corresponds to the best fits between the corrected and rescaled synthetics and the observed data.

In all above, the observed data time series start at the phase picks from MQS catalog (see Table 2) and are slightly adjusted separately between P and S to cover the body wave pulse. The duration of the windows are of 10 seconds, as a compromise between stability and the need to avoid contamination by later secondary phases as much as possible. In our approach, the ε weights have been chosen empirically to ensure a balance between quality of the fits and solutions stability at every depth (see the Section 5.1 for the final weighting values). According to our tests the PZ and ST synthetics are less sensitive to the model structure and consequently have an higher ε.

Table 2
Summary of the data phase arrival times for each marsquake. (1) arrival times derived from Khan et al (2021); (2) arrival times derived from Drilleau et al (2022); (3) S0820a secondary phases have not been picked yet in the current literature, the table arrival times are defined based on the mean arrival times of the nearby marsquakes S0173a and S0809a. The *P* and *S*-wave picks are stated in UTC time (time in the Earth reference frame, as YYYY-MM-DDThh:mm:ss) and secondary phases are expressed as differential times between them and body waves (in seconds).

	P-wave (UTC time)	*S*-wave (UTC time)	PP-P (s)	SS-S (s)	PPP-P (s)	SSS-S (s)
S0173a(1)	2019-05-23T02:22:58	2019-05-23T02:25:55	20	25	38	40
S0235b(1)	2019-07-26T00:19:21	2019-07-26T00:22:07	21	23	39	35
S0325a(1)	2019-10-26T06:59:01	2019-10-26T07:02:48	29	27	53	50
S0407a(1)	2020-01-19T09:57:47	2020-01-19T10:00:37	23	23	43	34
S0409d(2)	2020-01-21T11:31:29	2020-01-21T11:34:08	28	21	37	40
S0484b(1)	2020-04-07T08:52:39	2020-04-07T08:55:27	20	21	40	35
S0784a(2)	2021-02-09T00:16:20	2021-02-09T00:19:19	14	20	22	28
S0809a(2)	2021-03-07T11:13:16	2021-03-07T11:16:12	16	24	30	39
S0820a(3)	2021-03-18T14:55:33	2021-03-18T14:58:11	18	24	34	40

4.3.2. Secondary phase amplitudes

On the basis of the rescaled synthetics described above, we compute the amplitude ratios between synthetic secondary phases and direct body waves, and compare the value with the observed signals. Using Q_P and Q_S factors is likely a significant approximation as the PP, PPP, SS and SSS rays are not propagating at the same depths as the *P* and *S*-wave. We exclusively focus on the maximum amplitudes of the Z component of PP, SS, PPP and SSS, and their associated P and S maximums (*i.e.* PP over P, PPP over P, SS over S and SSS over S).

For example in the case of the secondary phase PP, the maximum amplitude ratio is calculated as:

$$\mathrm{Amp}^{\mathrm{PP}} = \frac{\max(\mathrm{d}^{\mathrm{PP}})}{\max(\mathrm{d}^{\mathrm{P}})}, \tag{6}$$

where $\mathbf{d}^{\mathrm{PP}}$ and $\mathbf{d}^{\mathrm{P}}$ correspond to the observed or synthetic time series on a 5-seconds window for PP and P phases, respectively.

The observed secondary arrival times are compiled in Khan et al (2021) and Drilleau et al (2022), summed up in Table 2 and computed with TauP toolkit (Crotwell et al, 1999) on synthetics.

4.4. Total cost function: solution selection

We select the best moment tensor solutions based on the lowest cost function value, which is the sum of eight separate terms; four terms on body wave fits of PZ, PR, SZ and ST, and four terms on secondary phase amplitude comparisons of PP, SS, PPP and SSS.

The synthetic body waves result from Section 4.3.1 computations, for each set of *Q*, M_0, τ and MT geometry. The body wave cost function χ is calculated with a root mean square (RMS) difference evaluation on the body waveforms for each body wave component:

$$\chi = \sqrt{\frac{\sum_i (\mathrm{d}_{\mathrm{syn}}(i) - \mathrm{d}_{\mathrm{obs}}(i))^2}{N}}, \tag{7}$$

where χ is computed at each point i over a 10 seconds window and N corresponds to the number of points (200).

From secondary amplitude computation in Section 4.3.2, we then compute the RMS difference κ between observed amplitudes and synthetic amplitudes with the equation:

$$\kappa = \sqrt{(\mathrm{Amp}_{\mathrm{syn}} - \mathrm{Amp}_{\mathrm{obs}})^2}. \tag{8}$$

The terms $\mathrm{Amp_{syn}}$ and $\mathrm{Amp_{obs}}$ account for maximum amplitude ratios of synthetics and observed data respectively (Eq. (6)).

Therefore, the total cost function Φ is the sum between χ (Eq. (7)) and κ (Eq. (8)). We weight each cost function terms with weights α and β and the sum of the total weight is 1, *i.e.* $\alpha + \beta = 1$:

$$\begin{aligned}\Phi \quad = \quad & \alpha\cdot(\chi^{\mathrm{PZ}} + \chi^{\mathrm{PR}} + \chi^{\mathrm{SZ}} + \chi^{\mathrm{ST}}) \\ & +\beta\cdot(\kappa^{\mathrm{PP/P}} + \kappa^{\mathrm{SS/S}} + \cdot\kappa^{\mathrm{PPP/P}} + \kappa^{\mathrm{SSS/S}}).\end{aligned} \tag{9}$$

A final constrain is applied to choose the best solutions. As there is a lack of clear surface wave observations in the InSight data, we are looking for solutions where the synthetic surface waves are weaker than the current observed data level.

In this end, we evaluate the ratio γ of the quadratic mean between the synthetic surface waves and the Martian noise, and of the observed surface waves, with the following equation:

$$\gamma = \left| \frac{\sqrt{\mathrm{SW}_{\mathrm{syn}}^2 + \mathrm{SN}_{\mathrm{obs}}^2}}{\mathrm{SW}_{\mathrm{obs}}} \right|. \tag{10}$$

SW corresponds to the spectra over the surface wave windows and *SN* is the spectrum of the data noise. The spectra are calculated on the Z component and filtered between 15 and 50 seconds (0.02–0.067 Hz). The surface waves window starts 100 seconds after the *S*-wave and last 90 seconds for both synthetic and data. The noise signal is selected in the 5-minutes window prior to the arrival of the *P*-wave from the MQS pick (InSight Marsquake and Service, 2021) and over a 90 seconds window. The solutions with γ ratios superior to 1 are rejected.

Note that once the total inversion process is completed for one event, we perform a secondary inversion. The evaluation of the source term in Eq. (1) is adjusted, where we implement the refined cutoff frequencies (Eq. (2)) calculated with the best M_0 (from Eq. (5)).

5. Inversion results

In this section we present the inversion results for the nine marsquakes. We first describe the inversion parametrization. We then show the S0235b results in a more detailed way in order to represent the complete computation for a single quake. Then, we summarize the results found for the whole dataset and we detail the preferred solutions per event. The complete overviews of the results for all the seismic events, from S0173a to S0820a, are described in Supplementary materials.

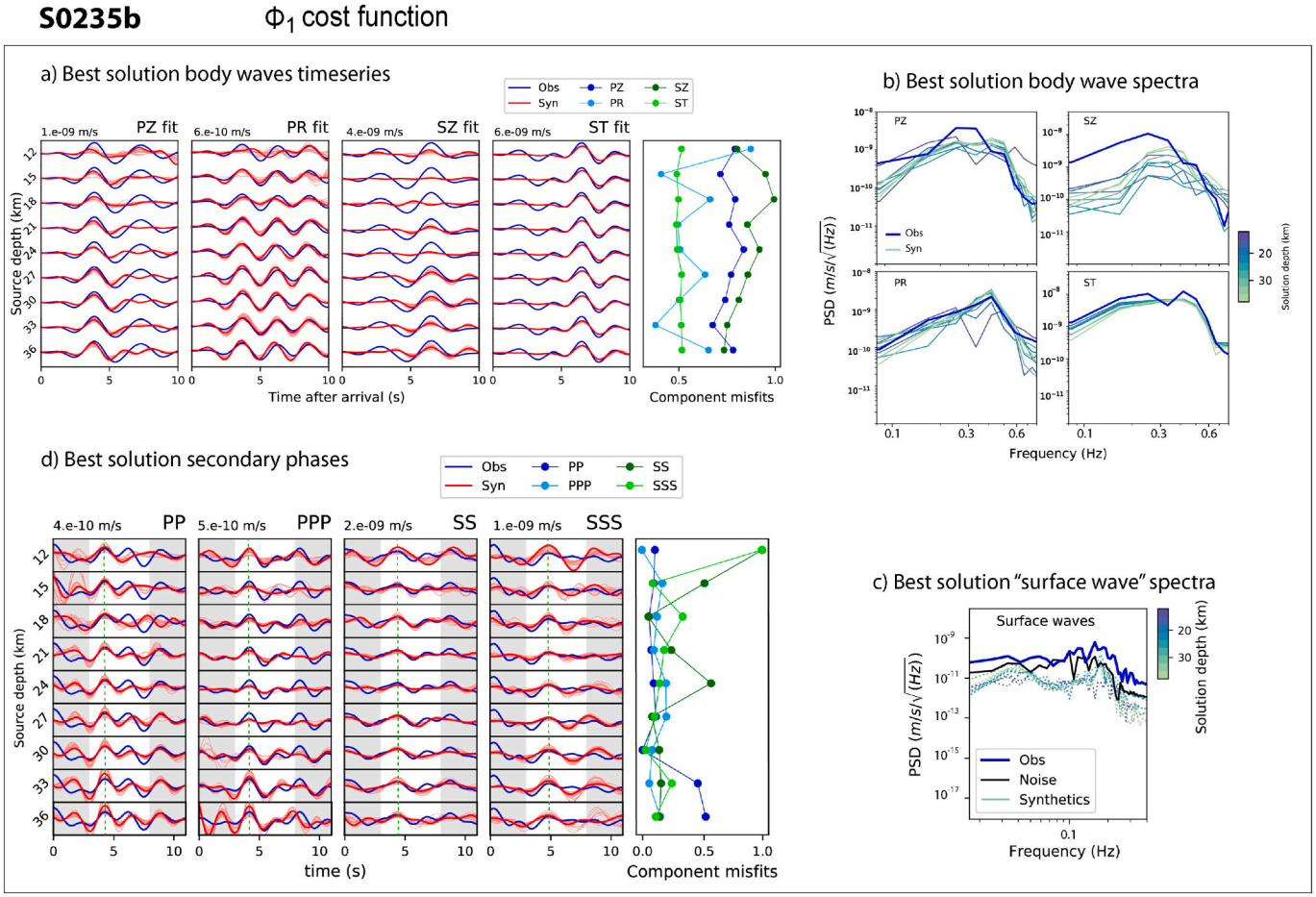


Fig. 3. Complete results for S0235b event for the Φ_1 cost function analysis. (a) best body wave fits, (b) best body wave spectra, (c) best solution surface waves spectra, d) best solution secondary phases. The colorcodes for (a) and (d) are the same; the blue signal corresponds to the data, the red signal corresponds to the best solution and the lighter red curves correspond to the 19 best synthetic solutions, the green dashed line on (d) is located at the secondary phase maximum and the gray areas are purely aesthetics and added for better readability. The body wave and secondary phase (white areas) windows start on arrival times of Table 2. The normalized misfit curves are displayed on the right panel of body wave fits and secondary phases, where PZ and PP misfits are in dark blue, PR and PPP in light blue, SZ and SS in dark green and ST and SSS in light green. Spectra on Figures (b) and (c) follow the same colorbar, along the depth; the shallow solutions are in indigo (12 km deep) and the deep solutions are in light green (36 km deep), the blue spectra correspond to the data and the black dashed line to the Martian noise preceding the event. The synthetic surface wave spectra are displayed in dashed lines. (For interpretation of the references to color in this figure legend, the reader is referred to the web version of this article.)

5.1. Inversion parametrization

In order to validate our method and its parameterization, we invert a terrestrial earthquake in a context comparable to the Martian conditions of InSight (intraplate earthquake, addition of Martian noise, velocity model of Knapmeyer-Endrun et al (2021), located at 1600 km epicentral distance on a 25 km thick crust). The resulting moment tensors with our single-station approach are in strong good agreement with the USGS (Guy et al, 2015) and the GFZ (Quinteros et al, 2021) inversions. The details of this inversion and the results of this test are available in Supplementary material S9. Besides, we also compute two sensitivity tests on the S0235b event; the sensitivity to the BAZ of the event (Supplementary material S10) and the dependency towards the velocity model (Supplementary material S11).

We have chosen the inversion weights according to the best compromise on the ratio of the weights in the variance η (ε in Eq. (4)) and in the total cost function (α and β values in Eq. (9)). For ε weights, we observe that the ratio of 0.4 on PZ and ST and 0.1 on PR and SZ is the

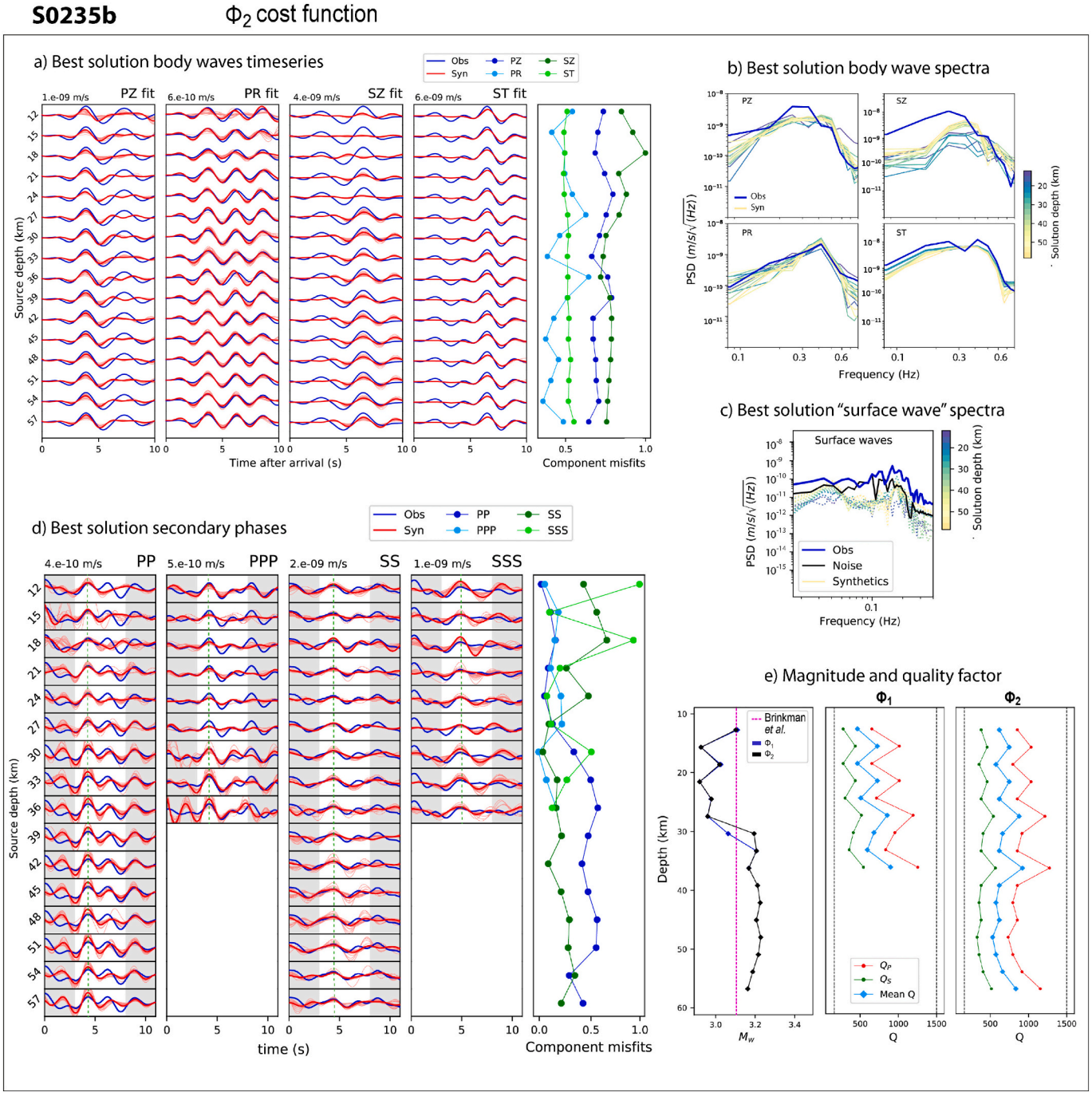


Fig. 4. Complete results for S0235b event for Φ_2 cost function analysis, in the same formalism as Fig. 3a best body wave fits, (b) best body wave spectra, (c) best solution surface waves spectra, (d) best solution secondary phases and (e) the best M_w along the depth on the left panel for both Φ_1 and Φ_2, and the best Q, Q_P and Q_S, for Φ_1 on the middle panel and Φ_2 on the right panel. On Figures (b) and (c) The spectra colors are shaded from indigo (12 km deep) to yellow (57 km deep). On left plot of (e), Φ_1 M_w is in blue, Φ_2 M_w is in black and the M_w value from Brinkman et al. (2021) is the pink dashed line. On middle and right panels of e), the red curves correspond to Q_P, the green curves to Q_S and the light blue curves account for the mean Q. (For interpretation of the references to color in this figure legend, the reader is referred to the web version of this article.)

most appropriate in order to obtain good fits on the maximum number of components as well as better solution stability. A ratio of $\alpha = 0.7$ on the body waves and $\beta = 0.3$ on the secondary phases is retained to account for the discrepancy in the number of points between body wave terms and secondary phases.

Furthermore, we make two cost function analyses (Eq. (9)) for all the marsquakes in order to investigate the stability of solutions at higher depths. Thus, we separate; i) Φ_1 as the full cost function results ($\alpha = 0.7$, $\beta = 0.3$), which encompasses the four body wave terms (PZ, PR, SZ and ST) and the four secondary phase terms of (PP, SS, PPP and SSS); ii) Φ_2 as the partial cost function, including the four body wave terms (PZ, PR, SZ and ST) and only the two secondary phase terms of PP and SS. This partial cost function Φ_2 is mainly used to explore deeper solutions as PPP and SSS are limited to $\sim$ 40 km depths.

5.2. S0235b event results

The 20 best body wave fits at each depth (over a total of 32000 solutions at each depth, between 12 and 57 km) are represented on Fig. 3a for the case of Φ_1 cost function terms, and on Fig. 4a for the case of Φ_2 terms. In these Figures, we calculate the body wave fits on the 10 seconds window on PZ, PR, SZ and ST components. We also display the associated misfits for each component, normalized separately between 0 and 1. We observe that the main energy peak is well retrieved on the four body wave components. Notably ST is very well constrained and has small and very stable misfits, although the first five seconds of signal are not retrieved in the calculation and the fits focus more on the main wavelength occurring after 5 seconds. This is explained by the fact that the maximum of the observed ST amplitude is located at about 5 seconds after the arrival of the *S*-wave, despite the first oscillation at $\sim$ 2 seconds. The synthetics are therefore rephased (from τ_p and τ_s, see Section 4.3.1) according to this maximum and ignore the first seconds of signal. Since we rephase all components of the *S*-wave with the same phase, the early signal is also ignored on SZ. Concerning the SZ component, the maximum pulse at 6 seconds is not well estimated for between 12 and 24 km depths. On the other hand in the case of the *P*-wave, the last 5 seconds of the signal are slightly underestimated for PZ and the main peak is well estimated. PR is very well retrieved at all depths except at 12 km depth for Φ_1 evaluation.

In addition to these Figures, the observations on the body waveform fits for the 4 components are consistent with the body wave spectra (on Figs. 3b and 4b). PZ, PR and ST components are well retrieved and in agreement with the data for both amplitudes and spectral shape. The SZ spectra are the least resolved, as the general shape of the spectra is shifted towards the high frequencies compared to the data and is strongly underestimated. As observed in the time domain of Figs. 3a and 4a, the SZ shallow depth solutions are the worst, with more than two orders of magnitude lower than that of the observed data. This is certainly explained by the weaker evaluation and the bad phase shift of the SZ waveforms in the first 5 seconds.

The synthetic surface wave spectra on the right panel of Figs. 3c and 4c are much weaker by about one order of magnitude than the Martian noise at all depths.

We represent the secondary phase amplitude results on Figs. 3d and 4d. On these, PP, SS, PPP and SSS timeseries are presented on a 11-seconds time window, where we add 3 seconds of signal (gray areas) before and after the effective secondary phase window. We display the normalized misfits on the right panels. The synthetic and observed waveforms are shifted according to their maximums (green dashed line) for better readability. From TauP computations, in the case of S0235b, the synthetic secondary phases PPP and SSS are not detected below 37 km (Φ_1 case), and SS are absent below 59 km (Φ_2 case). The secondary phase maximums are overally well retrieved at all depths and similar between Φ_1 and Φ_2 analyses. Especially, PP and PPP display small and stable misfits. SS and SSS are slightly less constrained. SS stabilizes below 24 km depth in both Φ_1 and Φ_2 cases. SSS is overestimated at 12 and 18 km depths.

We then visualize the magnitude M_w and quality factors Q_P for the *P*-wave and Q_S for the *S*-wave on Fig. 4e. The M_w and Q values globally are very similar between Φ_1 and Φ_2. The crustal M_w tends to 2.9. Below 30 km, the M_w is very stable and tends to 3.2. Our M_w values are in agreement with those computed in Brinkman et al. (2021) (value of 3.1, in pink dashed line), but underestimated compared to the MQS with values of 3.6 $\pm$ 0.2 (InSight Marsquake and Service, 2021).

The mean Q evaluation is oscillating from 12 to 57 km depth between $\sim$ 500 and 1000 (corresponding to Q_S values of 300–600) and are certainly related to the mean Q step of $\sim$40. The general shapes of the spectra on Figs. 3b and 4b are also affected by the attenuation value, which impacts the slope of the spectra. The higher the attenuation (*i.e.* Q is small), the flatter the spectrum is at high frequencies and the higher is the M_0 to compensate. In the case of S0235b, the 3 component spectra of PZ, PR and ST are quite reliable to the data, and thus we can expect that the attenuation is rather well estimated. Indeed it is coherent with Brinkman et al. (2021) values of $\sim$ 500, despite being overestimated compared to Giardini et al (2020) evaluation of 320.

On Fig. 5, we display the best moment tensor solutions for S0235b.

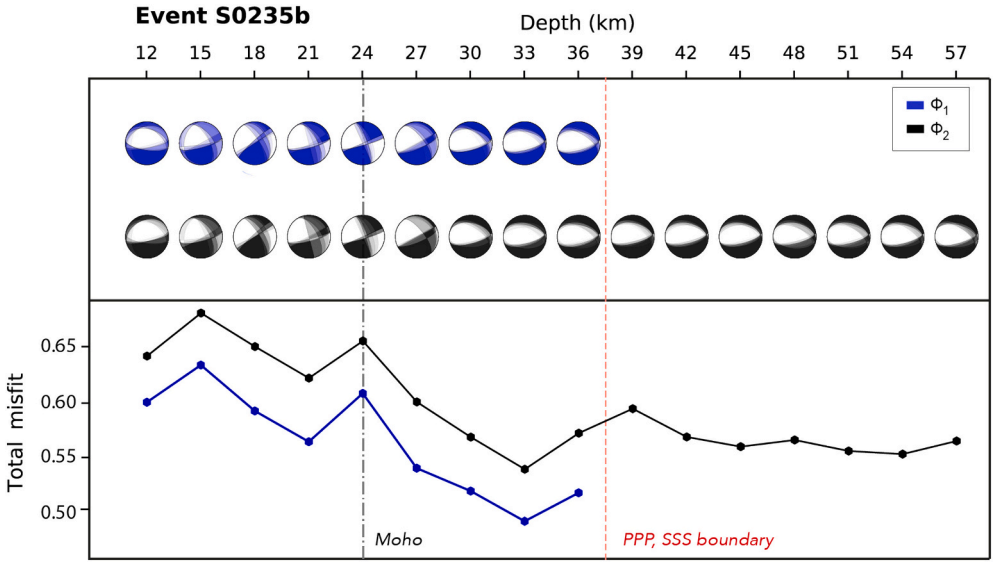


Fig. 5. Inversion result representations on the best moment tensor solutions of event S0235b. The Φ_1 cost function results are depicted with blue beachballs (top) and blue misfit curve (bottom) and the Φ_2 analysis results are illustrated in black. On the top panel, the 20 best moment tensor solutions, corresponding to the lowest total misfit computations, are displayed as probability density functions (PDFs) and along the depth. On the bottom plot, the total misfit curves Φ_1 and Φ_2 are shown for the best solution. The velocity model Moho depth is represented with a black dashed line and the PPP-SSS shadow zone boundary is represented with a red dashed line. (For interpretation of the references to color in this figure legend, the reader is referred to the web version of this article.)

On the top, we represent the moment tensor beachballs in a probabilistic formalism with a probability density function (PDF), where we superpose the 20 best solutions on top of each other. On the bottom, the total normalized misfits (equivalent to Φ_1 and Φ_2) are the sums of the different terms (body wave fits and secondary phase amplitudes). The focal mechanisms for S0235b are stable at each depth and also from one depth to another, below 30 km. A normal faulting regime is pretty well constrained from 12 to 57 km (with mixed strike-slip components at crustal depths), and strike and dip are constant with mean values of 80° (300° second nodal plane) and 65°(50°) respectively. Moment tensor results between the two cost function analyses are also very similar. In fact, we note that the moment tensors are a bit unstable in the crust either on the strike or the rake components (as observed on the body wave fits on top of Figs. 3a and 4a. These instabilities are certainly due to the temporal proximity of the depth phases (pP, sS) with the main peak of the body waves in the 20 first kilometers, as already evoked in Brinkman et al. (2021). It might also be explained by the close velocity model discontinuity at 10 km and at 24 km with the Moho (from Lognonné et al, 2020; Knapmeyer-Endrun et al, 2021).

5.3. Results summary

According to all our results (detailed in the Supplementary materials S1 to S8 for the complete dataset):

- The body waveforms are better constrained on the PZ, PR and ST components, while SZ is difficult to estimate in several cases (*e.g.*, S0235b, S0484b, S0820a, as well as in Brinkman et al. (2021) results on S0173a and S0235b). In fact, the SZ components are contaminated by larger converted receiver phases which do not facilitate the calculations.
- The secondary phases are well estimated on PP, SS and SSS, whereas PPP is frequently very weak in amplitude compared to the data for multiple events (*e.g.* S0407a, S0784a, S0809a). This can be partially attributed to the difficulty of observing PPP in a very small frequency band (Khan et al, 2021; Drilleau et al, 2022), but this also applies to PP identification, which are on the contrary better constrained in our computations.
- Magnitudes are stable in general, recurrently much smaller than those found by the MQS by about 0.5 (InSight Marsquake and Service, 2021 and Table 1), but in agreement with the values of Brinkman et al. (2021) for events S0173a and S0235b. This discrepancy is not fully understood at this time.
- In parallel, the Q factor is rather constrained overall. Still, it can converge to the limit values and not stabilize in depth (*e.g.* S0325a, S0409d, S0784a, S0809a). In this study, Q acts more as a tapering parameter on the spectral shapes and on the M_w evaluations, and does not affect the global geometry of the moment tensor solutions.
- Lastly, we find that synthetic surface waves are about one order of magnitude smaller than the observed data, and we have selected at least 90% of the global dataset solutions with surface wave amplitudes smaller than the InSight data (see S0235b spectra Figs. 3c and 4c. This implies that the Martian noise is high enough to exceed the synthetic surface waves even at 12 km. In other words, this finding is very valuable, as it leads to the conclusion that shallow sources at about 12 km depth are possible for all the inverted LF/BB events, despite the fact that there are no clear surface waves in the InSight data.

We represent the best moment tensor solutions for every marsquakes at each depth on Fig. 6 for Φ_1 cost function and on Fig. 7 for Φ_2 cost function. The majority of Φ_1 solutions have slightly better stability than those of Φ_2 on the same depths, and overall the tensors are in very good agreement between the two cost functions. Similarly to S0235b (Section 5.2) the crustal solutions between 12 and 21 km are frequently unstable with a succession of minimum-maximum misfit values (*e.g.* 18 km deep

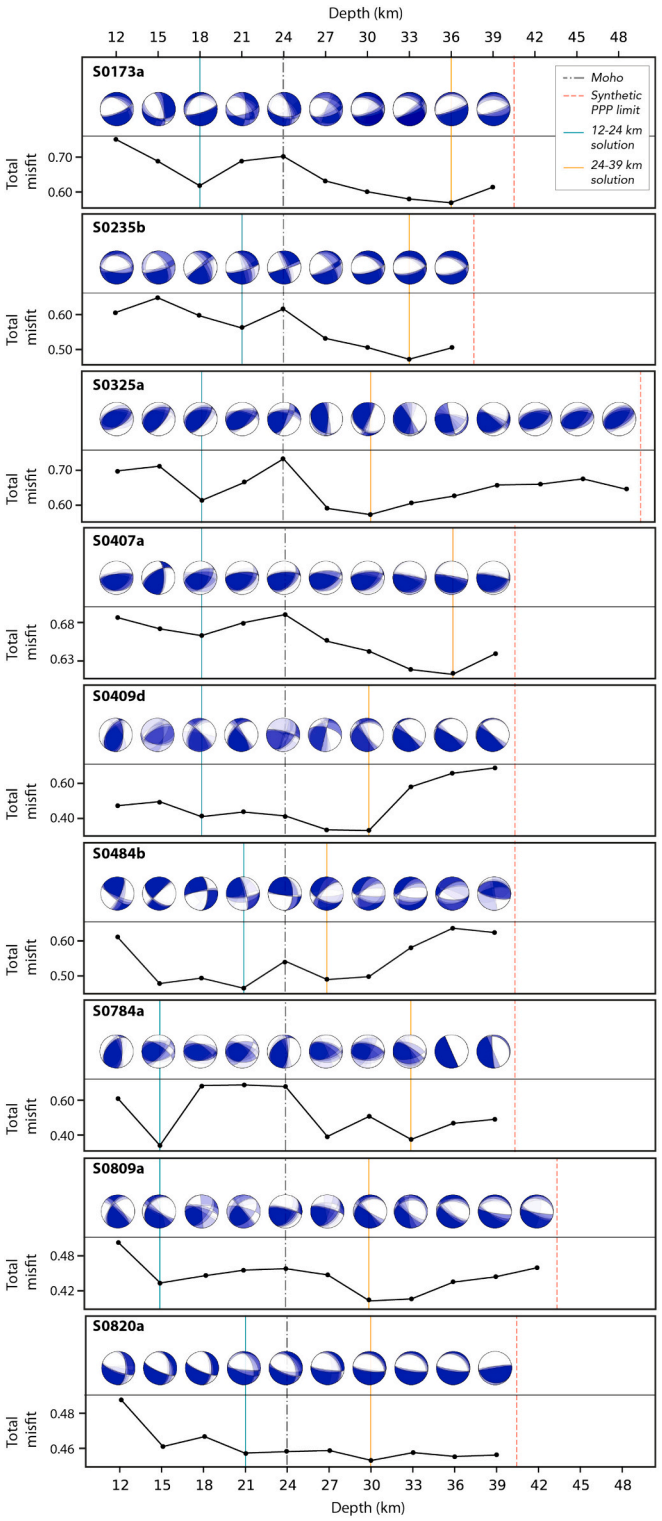


Fig. 6. Inversion result representations on the best moment tensor solutions for the nine events in the case of Φ_1 cost function analysis. At each depth, the 20 best moment tensor solutions, corresponding to the lowest total misfit computations, are displayed as probability density functions (PDFs). On the bottom plots under each PDFs plot, the total cost function curves Φ_1 are shown for the best solution. The velocity model Moho depth is represented with a black dashed line, the PPP-SSS shadow zone boundary is represented with a red dashed line and we highlight the selected solutions from Section 5.3 between 12–24 km (cyan) and 24–39 km (orange). (For interpretation of the references to color in this figure legend, the reader is referred to the web version of this article.)

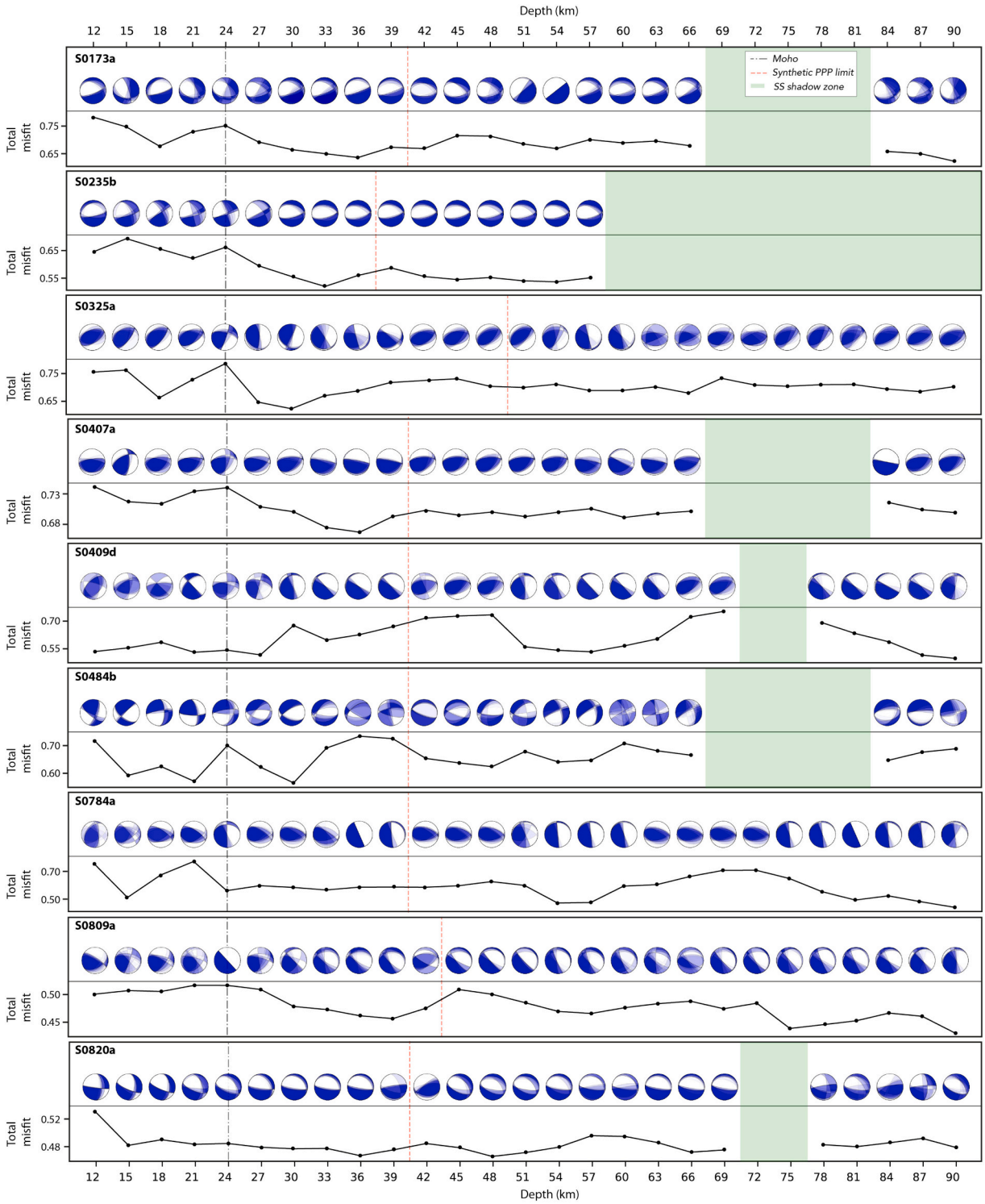


Fig. 7. Inversion result representations on the best moment tensor solutions for the nine events in the case of Φ_2 cost function analysis. We use the same formalism and colorcode of Fig. 6. The SS shadow zones are represented by the green areas. (For interpretation of the references to color in this figure legend, the reader is referred to the web version of this article.)

solution of S0173a on Figs. 6 and 7, and in Supplementary material S1). On these Figures, the six events S0173a (detailed in Supplementary material S1), S0235b (Section 5.2), S0409d (Supplementary material S4), S0484b (Supplementary material S5), S0809a (Supplementary material S7) and S0820a (Supplementary material S8) are characterized by normal faulting mechanisms at a majority of depths. S0325a (Supplementary material S2), S0407a (Supplementary material S3) and S0784a (Supplementary material S6) converge to a reverse mechanism. The S0409d, S0484b, S0784a and S0809a beachballs are unstable on several DC components along the depth. In addition, these events are the least resolved at each depth, meaning that multiple solutions resolve the data. The resulting PDFs are not as concentrated as those of the other seven marsquakes.

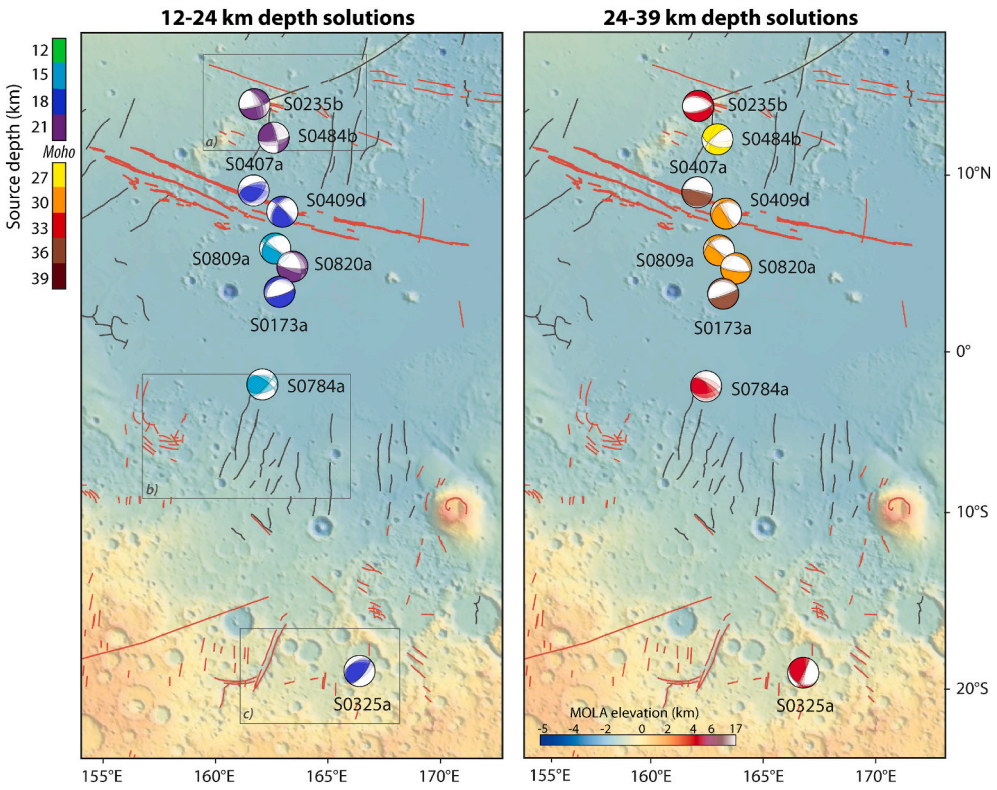


Fig. 8. Topographic maps of Mars (MOLA elevation) with the main tectonic features and centered on the selected moment tensor solutions for the nine inverted quakes. The compressive structures are highlighted in black lines and the extensive structures are in red lines (from Knapmeyer et al., 2006). Cerberus fossae faults are in thicker red lines (Perrin et al, 2022). The left map displays the shallower solutions between 12 and 24 km and the right map to the deeper solutions from 24 – 39 km deep. The focal mechanisms are located on their epicenters (from Fig. 1 and Table 1), and are displayed with probability density function of the twenty best solutions. Colors of focal mechanisms correspond to the exact solution depth: light green, blue and dark purple colors are associated with depths from 12 – 24 km and yellow, orange, red and brown colors with depths from 24 to 39 km. Three black squares (a), (b) and (c) on the left plot correspond to the zoomed map imprints of Fig. 9. (For interpretation of the references to color in this figure legend, the reader is referred to the web version of this article.)

Table 3
Best solution parameters described in Section 5.3. For each event, we display the dominant mechanism type (based on the first nodal plane rake angle value), the best solutions depths, the moment tensor strike, dip and rake angles, the magnitude M_w and the quality factors of P, Q_P, and S, Q_S. We highlight in bold the values of Q when Q_P tends to the extremity of the exploration domain (1500). The moment tensor components are displayed for the first nodal plane (auxiliary plane in parenthesis). The events first line corresponds to the 12–24 km solution mechanism and the second line for the 24–39 km solution (represented on Figs. 6 and 8).

	Dominant mechanism	Depth (km)	Strike (°)	Dip (°)	Rake (°)	M_w	Q_P	Q_S
S0173a	Normal	18	76 (219)	72 (22)	−76 (−113)	3.02	**1500**	**667**
	Normal	36	72 (246)	81 (10)	−89 (−95)	3.21	**1500**	**667**
S0235b	Normal	21	75 (330)	72 (54)	−110 (−83)	2.92	1035	460
	Normal	33	76 (283)	63 (54)	−104 (−77)	3.21	855	380
S0325a	Thrust	18	38 (245)	58 (36)	76 (113)	2.93	**1500**	**667**
	Thrust	30	130 (18)	27 (81)	94 (114)	3.24	840	373
S0407a	Thrust	18	246 (64)	54 (45)	104 (77)	2.23	635	282
	Thrust	36	280 (95)	81 (10)	91 (85)	2.51	773	343
S0409d	Strike-slip	18	313 (208)	76 (45)	52 (161)	2.35	1320	587
	Normal	30	152 (263)	81 (27)	−66 (−136)	2.17	442	196
S0484b	Strike-slip	21	102 (05)	76 (72)	18 (160)	2.44	1158	513
	Normal	27	111 (228)	49 (63)	−75 (−121)	2.61	759	337
S0784a	Thrust	15	45 (284)	68 (40)	67 (132)	2.52	1200	533
	Thrust	33	303 (87)	64 (27)	104 (66)	2.73	1257	559
S0809a	Thrust	15	313 (223)	86 (22)	66 (174)	2.62	1020	453
	Normal	30	123 (265)	68 (32)	−73 (−123)	2.96	420	186
S0820a	Normal	21	94 (249)	81 (14)	−85 (−115)	2.78	702	312
	Normal	30	98 (303)	72 (19)	−98 (−67)	2.83	873	388

5.4. Best source solutions

On both result Figs. 6 and 7, there is no trend of a minimum misfit for the entire set of events, with one depth standing out. The previous work on Martian moment tensor presented by Brinkman et al. (2021) for events S0173a and S0235b (and S0183a) agrees on depths on the order of 33–40 km. Also, Drilleau et al (2022) find source depths of 20-35 ±10 km for all the events (except S0820a which is not analyzed in their study), based on depth phase observations. Moreover, the synthetic secondary phases PPP and SSS identified in the data are calculated with the TauP toolkit (Crotwell et al, 1999) on the synthetics up to 40 km depth.

From these, in order to remain consistent with data and recent results, we assume that the seismic sources are located at depths between 10 and 40 km. We propose to select two Φ_1 solutions for each event; one in the crust between 12 and 24 km and the other under the equivalent Martian Moho of the velocity model, between 24 km and until the shadow zone depth of synthetic PPP-SSS of about 40 km depth. We choose the sets of solutions based on the misfit minimums on Φ_1, and the moment tensor solutions must be similar between Φ_1 and Φ_2.

We display on Fig. 8 the two selected moment tensor solutions for each quake (also highlighted with blue and orange lines on Fig. 6). The figure is separated into two topographic maps gathering the large surface structures of the study area (Knapmeyer et al., 2006); on the left

panel we represent the crustal solutions between 12 and 24 km deep, and on the right panel we show the solutions between 24 and 39 km deep. Each moment tensor solution is located at the epicenter of the event, *i.e.* at the center of the ellipsoid (visible on Fig. 1). In parallel, the Table 3 summarizes the set of output parameters associated with each solution, specifying the type of the dominant focal mechanism, the depth of the source, the three angles of the strike, dip, and rake, and the calculated magnitude M_w and attenuation factors of Q_P and Q_S.

Analyzing the selected solutions on both Fig. 8 and Table 3, we first observe that S0173a, S0235b and S0820a marsquakes are in the normal dominant regime (mixed with strike-slip components for S0409d and S0484b), on the other hand, S0325a, S0407a and S0784a display clear reverse regime. Lastly, the dominant regime of S0809a is not obvious because its rake is unstable, either reverse in the crust, or normal at higher depths.

The majority of the selected sources are located at 18 and 30 km depths. The depth values of our results for S0173a, S0235b, S0325a, S0409d, S0484b and S0809a are very close to those obtained in Drilleau et al (2022) from pP and sS depth phase analyses. The S0173a solution at 36 km depth and the S0235b' 33 km solution are very similar to the depths of ~ 30–35 km from Brinkman et al. (2021).

Events S0173a, S0235b, S0407a, S0484b and S0820a have stable and similar strike angles oriented towards E-W/NW-SE. The thrust fault mechanisms of S0325a, S0407a and S0784a are also oriented E-W globally, but with less similarities between them as they are not located in the same area.

The dip angle is remarkably similar for the nine marsquakes, with high values of 70–80° on their first nodal plane. Excepted in the cases of S0235b and S0484b, the dip angles are asymmetrical between the first and the auxiliary nodal planes, the second plane being much less inclined (values approximately between 10 and 40°).

The rake angle varies significantly between events, with values ranging from −76° (S0173a) to −115° (S0820a) for normal events, and from 67° (S0784a) to 132° (S0784a) for reverse ones. S0809a is peculiar and its rake at 15 km depth is mixed between right-strike-slip and thrust motion, while it is more clearly converging towards normal motion at 30 km depth.

The magnitude ranges between 2.17 (S0409d) and 3.24 (S0325a) with a majority of values around ~ 2.7. For all the events, the magnitude increases by about 0.2 at depth. The values are much lower than the MQS estimates including errors (InSight Marsquake and Service, 2021 and Table 1) to within 0.5, especially S0409d magnitude values which are more than 0.8 weaker than the MQS M_w values of 3.2 ± 0.2. Besides, the M_w of 2.92-3.21 of S0173a and S0235b are very close to the estimates of 3.0 and 3.1 respectively calculated by Brinkman et al. (2021).

Finally, the best solution quality factors Q_P and Q_S are not easily interpretable. Still, from our results, we observe the Q_S factor being mainly between ~350 and 500 (Q_P between ~800 and 1200), overestimated compared to the values from Giardini et al (2020), where the Q_S is of 300–320 for S0173a, S0235b and S0325a, but in agreement with the values imposed in Brinkman et al. (2021). The solutions of Q_S for S0235b and S0325a (30 km solution) are in good agreement with their study, as well as S0407a, S0484b (27 km solution), S0809a (15 km solution) and S0820a. The Q of S0173a is unconstrained and tends towards higher boundary at the two selected depths. Moreover, the values of Q can affect the M_w estimates, *i.e.* large Q factors result in underestimation of M_w.

6. Discussions

We have selected two moment tensor solutions for the nine inverted marsquakes. In this section, the solutions are interpreted in relation to the structures and the geological context of the region. We first highlight the different uncertainties and limitations of our inversion approach. Then we describe the generic structures of interest in the area. Finally, we make a more precise analysis on regions close to the epicenters, thus exploring several possibilities on the origin of the marsquakes.

6.1. Inversion limitations

In this study, we face difficulties coming from the numerous uncertainties and unknowns on Mars and due to the quality of data (single seismic station framework).

From the velocity model used to compute synthetic seismograms, we made the hypothesis that the crustal structure defined for the vicinity of the InSight station, recovered in Knapmeyer-Endrun et al (2021) from receiver function and auto-correlation approaches, is the same at the nine epicenters, which are situated 1000–2000 km away. In the same way, the 1D structure assumption implies that there is no lateral velocity (or density) heterogeneities and no variations of the Martian Moho depth (*e.g.* 24 km in the used model versus 35–40 km in the Cerberus region, from Parro et al, 2017 or Plesa et al, 2018). This inference is even more problematic for the event S0325a located on the Martian dichotomy. To address this issue, we invert an earthquake located in Australia with Martian synthetics (see Supplementary material S9) to show the non-dependence of the geometry of the moment tensors with the internal model. We also invert S0235b with the secondary crustal model from Knapmeyer-Endrun et al (2021), with a 3*rd* layer at 43 km (in Supplementary material S11). The moment tensor solutions of the Australian earthquake are very consistent with those calculated by the USGS (Guy et al, 2015) and the GFZ (Quinteros et al, 2021), and show good stability at depth. However, the magnitude (too small) and the quality factors (too high) are unconstrained due to their dependencies towards the velocity model. At the same time, the moment tensor results of the S0235b sensitivity test with 3-layered TAYAK model are quite similar to those of the 2-layered model (results in Section 5.2) but are less clearly extensive and are less stable over the full depth ranges. An accurate 3D model (that are recently being proposed, for example in Plesa et al., 2021) associated with 3D synthetics, or failing that, a model at the source location, would account better for the complexity of the internal structure.

We also have uncertainties on the localization of the marsquakes (distance and BAZ). Currently, the distance of the marsquakes is known to within approximately 5° (~ 300 km) uncertainties. In our methodology, we select separately the seismic phase windows, hence we can get rid of their relative arrival times controlled by the epicentral distance. Although, the synthetic amplitudes are directly dependent of the distance, and directly linked to the M_w and Q evaluations. Moreover, the sensitivity test on the BAZ (Supplementary material S10) demonstrates good stability overall. Yet, we note some differences in the moment tensor dip angles, with those of the nominal inversion of S0235b (in Section 5.2).

In addition, the uncertainty about the Martian structure is not only limited to layer geometry and heterogeneities but also to key parameters such as the attenuation (or $1/Q$). It controls the marsquake frequency content and the signal amplitude, and it is still not well understood and estimated for Mars. That is why in our approach it is one of the explored parameters, mainly used to adjust the fits of the body waves. But we are not able to find an emerging value for the nine marsquakes, and for instance in the case of S0325a (Supplementary material S2), the Q exploration tends towards the upper boundary. Its refinement would certainly allow to obtain optimal fits and a better estimate of the moment magnitude, as well as stress drop and fault size scales.

Finally, regarding the seismo-tectonic analyses that we make below, we are on a fairly well covered area both by satellite imagery and by scientific studies of recent years. However many structures are still poorly observed (for instance Al Qahira Vallis and Avernus Dorsa, see Figs. 1 and 9 and Section 6 below), and we lack field data to refine the remote morphological observations. A closer temporal monitoring between images of the same area (on the order of a day) would be also very useful to detect surface movements,*e.g.* landslides or boulders possibly related to the seismicity.

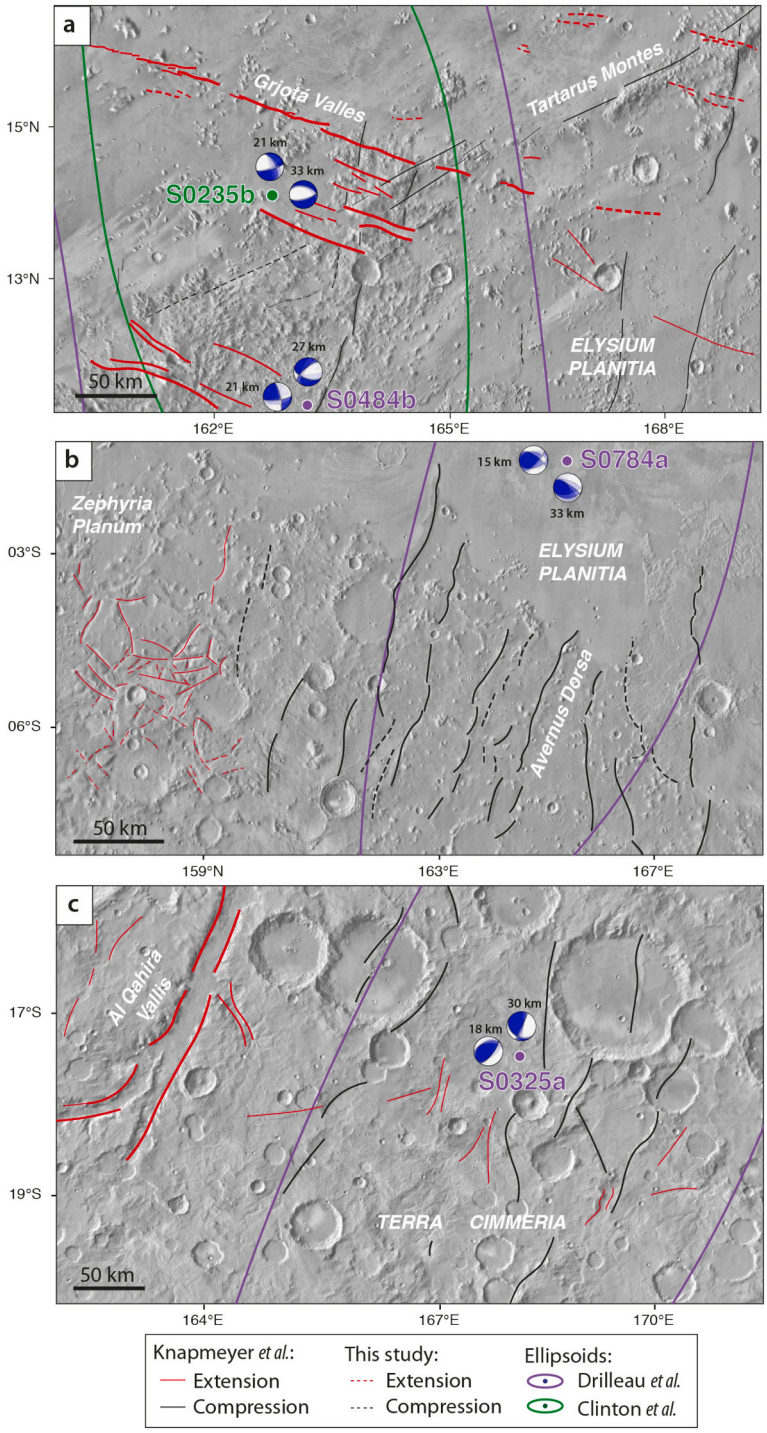


Fig. 9. THEMIS images (Fergason et al, 2006) of the tectonic structures and potential seismic sources in the vicinity of inverted marsquakes. The selected focal mechanisms (Fig. 8) are represented with their source depths and plotted at their epicenter locations (purple ellipsoids from Drilleau et al, 2022 and light green ellipsoids from InSight Marsquake and Service, 2021, Fig. 1 and Table 1). The tectonic structures are displayed in black lines (compressive structures) and red lines (extensive structures). The solid lines are derived from Knapmeyer et al. (2006), and the dashed lines represent these study mappings. The line thickness increases as the fractures and faults are well expressed on the orbital data. (a) corresponds to the S0484b and S0235b events zoomed on Grjotá Valles region, (b) corresponds to S0784a event in Avernus Dorsa and (c) is located at the dichotomy for S0325b. (For interpretation of the references to color in this figure legend, the reader is referred to the web version of this article.)

However, despite these difficulties, we have several studies that converge on the same results, using different approaches. Moreover, we are fortunate to have sufficiently high resolution images to look at the main structures. We are thus able to link our results to satellite observations.

6.2. Seismogenic sources

The most visible structures of the central Elysium Planitia region are fractures and faults, ranging from a few tens of kilometers to several hundred kilometers long. On all of our maps (Figs. 1 and 8) from Knapmeyer et al. (2006) data, two main modes of deformation are observed, extension (red lines) which is dominant in the region, and compression (black lines).

Notable extensional structures near the marsquakes are: the Cerberus fossae and Grjotá Valles systems, Elysium Fossae further north and Al Qahira Vallis at the dichotomy (Fig. 1). Cerberus fossae is suggested to have had tectonic activity as recently as 10 Ma (Vaucher et al, 2009; Taylor et al, 2013), and of a few Ma for Grjotá Valles (Hartmann and Neukum, 2001). Elysium Fossae activity is thought to be older, estimated at 200–500 Ma (Vaucher et al, 2009). Al Qahira Vallis is an ancient valley with several hundred million years of activity, between the last 2 Ga and 700 Ma ago (Cabrol et al, 1998).

The largest observed compressive structure in our area is located at

Tartarus Montes. It is a large ridge whose formation predates that of Grjotá Valles (Hamilton et al, 2010). All other compressive features of the region are of more moderate size and are mostly wrinkle ridges (for example, black lines in Avernus Dorsa). The wrinkle ridges are the result of lithospheric flexure and located at the apex of reverse faults at depth (Banerdt et al, 1982; Head et al, 2002).

6.3. Cerberus fossae: a major fracture zone in Elysium Planitia

In the study area on Figs. 1 and 8, Cerberus fossae is the largest structure, and is associated with the Grjotá Valles system further north. These two sub-parallel fracture zones are trending N100-110°E. They are good candidates as the source of the seismic events, suggesting an ongoing localized activity on Mars. From our results on Fig. 8 and Table 3, the seismic events S0173a, S0235b, S0409d, S0484b, S0809a and S0820a are associated to extensional moment tensors compatible with Cerberus extensive motion, while S0407a depicts reverse tensors and S0809a is both reverse (crust) and normal (deeper). Given the locations and diversity of the focal mechanism solutions, it is more likely that there are multiple seismic sources generating the seven marsquakes.

In more detail, the recent tectonic activity in this region could result from several processes involving thermal contraction and/or indirect volcanism. Recent volcanism in the last million years in the center parts of Cerberus fossae has been proposed by Horvath et al (2021) as recent as 50 ka. Moreover, some small amplitude and long duration LF events located on Cerberus fossae have been suggested as potential slow seismic events by Kedar et al. (2021). The existence of these slow marsquakes could imply that a seismic source by volcanism exists in Elysium Planitia. More recently, small events possibly associated with S0173a and S0235b have been proposed to be related to volcanic activity in the upper mantle by Sun and Tkalčić (2022). There is no direct evidence from gravimetric data that a mantle plume lies beneath Elysium Mons, whereas, a positive Bouguer anomaly of 100 mGal (about −100 mGal on the surrounding terrains) is visible near Avernus Dorsa (Genova et al, 2016, and see Figure in Supplementary material S12), possibly testifying to a less dense crustal mass, for example of magmatic origin. Besides, the infrared imagery from THEMIS data (Fergason et al, 2006) does not show localized hotspots along Cerberus Fossae faults, suggesting that there is currently little or no thermal anomaly related to a surficial magmatic flow. Thus, a shallow magmatic source is unlikely, but it is possible that a magma flow at depths exists (Kedar et al., 2021; Sun and Tkalčić, 2022).

On the other hand, the seismicity could rather be related to ancient dike networks at depth (≈ 5–20 km), as it is expected that they are radially distributed around the Elysium Mons volcano (Ernst et al, 2001). Despite the fact that Cerberus fossae and Grjotá Valles are located more than 1000 km east of the volcano, Ernst et al (2001) concluded on networks that may extend over distances of the order of more than 2000 km. Thus, these massive dikes are suggested to propagate under Cerberus fossae and Grjotá Valles systems, and are likely responsible for the graben subsidence (Vetterlein and Roberts, 2010; Taylor et al, 2013; Perrin et al, 2022). Rivas-Dorado et al (2021) analyzed the graben widths, lengths and topographic data, and inferred the relationships between dike depths and graben widths.They estimate that dikes can expand to depths from 5 – 20 km in the case of Elysium Fossae. We assume a similar configuration on the dike depths for Cerberus Fossae, as the graben widths are comparable with those of Elysium Fossae (Taylor et al, 2013; Perrin et al, 2022). The formation and propagation of dikes in depth is thus likely related to mechanical weakness and the creation/reactivation of adjacent sub-parallel fractures. It is therefore proposed that buried fractures exist below the graben systems, in the same geometry. In addition, the dip angles of the seven marsquakes are of the order of 60 to 80° (Table 1), thus sub-vertical, and more consistent with underlying extensional fractures. We also find most of our best moment tensor solutions around 18 km deep for all of the inverted masquakes (Fig. 8). Although these depths are on the same scale as the lower dike tips at 20 km of Rivas-Dorado et al (2021), it is unclear to relate our results directly to the movements generated by the grabens located at the top of the dikes, on the first kilometers. We note that S0173a, S0409d, S0809a and S0820a are well aligned together (mainly NW-SE oriented) and very close to the general direction of the Cerberus fossae grabens. Thus, we suppose that these marsquakes are indirectly associated to the Cerberus fossae tectonics, and instead originated from the reactivation of deep extensive fractures, resulting from dike emplacement. In the case of S0809a at 15 km depth, the moment tensor solution has mixed components of reverse and strike-slip while having comparable strike and dip angles with the 30 km deep solution. Therefore, to explain this, we suppose that a network of compressive fractures also exists, and accommodates the mainly extensive deformation of the dikes. But alternatively, the solutions may simply be unresolved, knowing that the crustal mechanisms of S0809a are otherwise not very stable (see Fig. 6 and Supplementary S7), in which case the extensive solution at 30 km depth would be favored.

From the mapping of Knapmeyer et al. (2006) (Figs. 1 and 8), there are no major compressive structures recorded at the ellipsoid of S0407a, and very few in the vicinity of Cerberus fossae fractures. The 18 km solution (NE-SW, with a small dip angle) is not obviously coherent with Cerberus fossae configuration, while the 36 km depth solution is in strong agreement with the system geometry (on both strike and dip angles). We thus propose that S0407a could be generated by buried thrust faults sub-parallel to Cerberus fossae. It is also possible that, given the location and tensor geometry of this event, it could be a reactivation by thermal contraction of the Cerberus fossae faults in reverse regime.

To the same extent, S0235b and S0484b are consistent with the geometry and tectonic activity of Cerberus fossae. Although, their epicenters are not located on Cerberus fossae, but are closer to the Grjotá Valles system. Thus, we can not clearly rule out one or the other system as a source for these marsquakes (see discussions in Section 6.4.1 below).

6.4. Analyses of other nearby seismic sources

Even though Cerberus fossae is clearly the largest structure in the region shown in Fig. 8, the nine seismic events are not all located on the fractures and/or their solutions are not all compatible with the graben geometry. In addition, the ellipsoids are the representations of the probability of the location of marsquakes with the epicenter being the highest probability, but the areas covered are broad (about 60,000–200,000 km^2 per event) and include several other major and moderate structures (as seen on Fig. 1). The sensitivity test results on the BAZ in Supplementary S11 demonstrate the robustness of the moment tensor solutions. Hence, we explore the remarkable structural features covered by the ellipsoids and investigate the possible other scenarios that would explain the source of the most distant marsquakes.

For this reason, we regroup on Fig. 9 three areas of interest of four marsquakes (see also insets referenced in Fig. 8), with their associated best moment tensor solutions and ellipsoid imprints: the S0235b and S0484b events along the Grjotá Valles (Fig. 9a and detailed in Section 6.4.1), the S0784a event along the Avernus Dorsa wrinkles (Fig. 9b and Section 6.4.2), and the S0325a event at the dichotomy (Fig. 9c and Section 6.4.3).

6.4.1. S0235b and S0484b: Grjotá Valles and Tartarus Montes region

In the cases of S0484b and S0235b, the ellipsoids are centered mainly on the Grjotá Valles system, north of Cerberus fossae (Figs. 1 and 9a). The Grjotá Valles grabens (shown in thick red lines) are proposed to be contemporary with the Cerberus fossae fractures (Vaucher et al, 2009; Brown and Roberts, 2019) because they intersect the same lava plains and flow channels. The system of Grjotá Valles has the same general orientation of N110°E and is radially oriented with respect to Elysium Mons. Thus, the Grjotá Valles and Cerberus fossae grabens most likely originate from the same processes, *i.e.* they would be the surface

expression of underlying dikes (Ernst et al, 2001; Brown and Roberts, 2019). In addition, the fractures intersect knobby terrains of the Noachian-early Hesperian (4.1-3.5 Ga, Hartmann and Neukum, 2001; Plescia, 2003; Vaucher et al, 2009) of the Tartarus Montes formation. Despite unlikely recent activity (Hamilton et al, 2010), the major compressive Tartarus volcanic ridge (solid black lines trending N60°E on Fig. 9a, has certainly enabled shallow fracturation in the region. We also observe a few minor N-S trending compressive structures of 20–50 km long that could be reactivated (thin black lines).

Given the normal fault solutions of the moment tensors selected for S0235b-S0484b (Fig. 8), we favor a seismic source located on either one of the Cerberus or Grjotá grabens. Especially, the S0235b strike angles of ~300° and of ~110° for S0484b solutions match very well with the overall graben directions of the two regions. As developed before in the case of Cerberus Fossae events, the seismic sources are more probably linked to internal weakening, oriented and aligned with Grjotá fractures, and without clear surficial imprints. The retained depths of S0235b are slightly higher than those of S0484b (33 and 27 km respectively) as well as the higher value of M_w of 2.9-3.2 versus 2.4-2.6 respectively. These inferences suggest that S0235b is associated with a larger and deeper structure than S0484b. Besides, the depths of these two events are too high to be related to a dike, but are more consistent with deep fractures or faults. This is also supported by their large dip angles of 60 −−70°, coherent with sub-vertical buried fractures. The lower dip angles of S0235b and S0484b (49–63°) at 33–27 km depth respectively, might suggest that the faults become slightly more listric at depth. We also note that the 21 km deep focal mechanism of S0484b has a large strike-slip component, which could imply an interaction between the extensional component at Grjotá Valles and the transpressive inherited NE-SW structures at Tartarus Montes (Fig. 9a). But this hypothesis would need further work, *i.e.* detailed observations on the morphology and geology of the area, to understand such complex interactions.

Further north of the S0484b ellipsoid (on top of Fig. 1), the Elysium Fossae graben is unconsidered as a primary seismic source due to an activity dated anterior to 200 Ma at most (Vaucher et al, 2009) and due to its location. In addition, we do not observe any particular extensive structure crossing the lava plains at the southern end of the S0484b ellipsoid (shared with the upper part of the S0784a ellipsoid, see the discussion below and Fig. 9b).

6.4.2. S0784a: Avernus dorsa ridges

The northern part of the S0784a ellipsoid (observable on the upper part of the Fig. 9b) is located on a broad volcanic plain of Elysium Planitia composed of Late Amazonian lavas (several hundreds of ka, Tanaka et al, 2011). On the mapping of Knapmeyer et al. (2006) on Figs. 1 and 8, we do not notice any surface fractures in these plains. However, gravimetric analyses (Genova et al, 2016) of the area shows that a positive Bouguer anomaly (300 mGal versus 0 mGal in the surrounding terrains, see figure in Supplementary material S12) exists at the northern end of the ellipsoid of S0784a, indicating a potential excess of crustal mass of a size of about 100 km which is not reflected in the topography. The mass excess is compatible with an upwelling of a denser mantle material, also compatible to a shallow dike activity, and supports a potential hidden activity below the lava deposits. But, even if the S0784a epicenter is located on these lava plains, the lack of information on a potential buried structure prevents us from favoring a source in these surroundings.

In addition, we observe a chaotic fracture network on the west outside of the event ellipsoid, mainly with moderate extensive fractures (red lines on Fig. 9b) of 10–50 km long without any preferential orientation. These extensive fractures could be subjected to compressive reactivation by the planetary thermal contraction. The S0784a solutions may be compatible with the E-W orientation of these chaotic fractures, although they are too distant (~ 400 km from epicenter) and principally extensive.

Besides, in Fig. 9b we show the main structures of the southern part of the ellipsoid. In the center of the figure, we highlight the sub-parallel wrinkle ridges of Avernus Dorsa trending NNE-SSW and dated late Noachian-early Hesperian (about 3.5 Ga, Tanaka et al, 2011). As the generic Martian wrinkle ridges, they are associated to regional shortening, and from mixed process between the regional volcanic strains (Watters, 1993; Mangold et al, 2000) and the brittle lithosphere contrast between Martian highlands and lowlands (Frey et al, 2002).

The solutions we compute for S0784a marsquake are mainly reverse (Fig. 8 and Table 3). The two solutions at 15 km and 33 depths are oriented E-W. Despite the fact that the reverse motion, the dip angles and depths of S0784a are in agreement with the wrinkle ridge geometries, the general E-W orientation of our two solutions is not in line with the NNE-SSW orientation of Avernus Dorsa traces. In contrast, S0784a is close to the dichotomy, and our solutions are oriented perpendicular to the southern highlands. At this transition zone, structures and cracks are also aligned with the dichotomy boundary, some of them are normal, and would have allowed the ancient subsidence of the lowlands (Maxwell and McGill, 1988; Smrekar et al, 2004). Thus, this deformation transmitted from the southern highlands in Terra Cimmeria to the northern lowlands of Elysium Planitia could have generated large crustal weaknesses and faulting (Frey et al, 2002; Golombek et al, 2018; Pan et al, 2020). It is therefore suspected that E-W oriented fractures, without surface expression, may exist in these deformed terrains. Thus, we propose that event S0784a may have been generated by a deep fault, parallel to the dichotomy and in a compressive regime, reactivated by the stresses associated with planetary contraction.

6.4.3. S0325a: The dichotomy region

In Fig. 9c, we identify the structures located in the center of the S0325a ellipsoid, within the cratered Terra Cimmeria terrains of Noachian age (about 4 Ga, Tanaka et al, 2011). The terrains are very old and cratered, and the wrinkle ridges present in the area intersect them. The relative chronology suggests that more recent activity is possible in this area, although highly uncertain and in the last 4 Ga.

On the northern end of the ellipsoid (Figs. 1 and 8) most of the deformation compiled by Knapmeyer et al. (2006) is extensional, and the fractures are weakly marked and of a few tens of kilometers long. The southern limit of the S0325a ellipsoid (Fig. 1) is adjacent to a small network of compressive fractures of variable orientations (note also that a large crack of about 50 km in an extensive regime oriented NE-SW has been mapped close to the southern end of the S0325a ellipsoid on Fig. 1 and compiled in Knapmeyer et al. (2006), but we consider this trace as erratic, as it is not corresponding to any clear surface expression). The center of S0325a ellipsoid is located 100 km east from a major structure, Al Qahira Vallis (Figs. 1 and 9c) which is an ancient valley oriented NNE-SSW. This structure is suggested to have been active between 700 Ma-2 Ga ago (Cabrol et al, 1998) and related to regional catastrophic overflow of a paleolake (Irwin et al, 2004). The general orientation of Al Qahira Vallis is rather N–S, but could be in agreement with the solutions of S0325a whose strike are of ~ 20–40° (Table 3). Although, the moment tensors of S0325a are mostly reverse whereas Al Qahira is a graben structure. In addition, the valley is located too far from the ellipsoid to be directly involved in this event. However, it is possible that the extension of Al Qahira Vallis generated other adjacent fractures closer to the ellipsoid. But without more information we cannot relate this major structure to S0325a with confidence.

On the other hand, in the center area of Fig. 9c inside the ellipsoid, we observe several wrinkle ridges (and a few small extensive fractures) oriented NNE-SSW/NE-SW and of the order of 50 km in length. The thermal contraction is supposed to be the main process at the origin of these contractional features.

The two S0325a moment tensors solutions at 18 and 30 km depths, are oriented NNE-SSW, with low to high dip angles (from 27–36° to 58–81°) and depict a reverse regime (Figs. 8 and 9c), consistent with most of the compressive features of this area. The 18 and 30 km solution depths are large, relative to the assumed depths of 1 to 10 km of the

thrust faults beneath the wrinkle ridges (Mangold et al, 1998; Schultz, 2000; Watters, 2004). But still, the geometry of wrinkle ridges is quite complex, and several studies actually mention crustal or lithospheric depths for wrinkle ridge fault rooting, depending on the brittle-ductile transition (Golombek et al, 2001; Montési and Zuber, 2003; Andrews-Hanna, 2020). Moreover, in Andrews-Hanna (2020), the tectonic modeling of wrinkle ridge morphology shows that additional faults are nucleated adjacent to the main blind thrust fault (dip angles of 20–70° up to 20 km depth), which can be rooted to depths up to 30 km beneath the ridges where it is listric (dip angles of 15–40°). The solutions on the dips, rakes and depths of S0325a event, are then consistent with wrinkle ridge geometries. On the other hand, we consider that S0325a tensors are the least stable of our dataset, the two solutions are very different from each other, and that the crustal model does not include the heterogeneities of the dichotomy highlands. In order to properly account for these limitations, we conclude that S0325a was generated by a reverse fault at depth reactivated by thermal contraction, and the fault could either be located under a wrinkle ridge, or merely be the result of the large regional deformation without surface expression.

7. Conclusion

InSight single seismic station on Mars requires inversion approaches specifically adapted to Martian data. We have thus developed a method of inversion of seismic moment tensors and applied it for nine marsquakes, to identify the probable seismic sources at their origin. For this purpose, we inverted the waveforms of the body waves P and S, and the amplitudes of the secondary phases PP, SS, PPP and SSS. We also selected the solutions with weak synthetic surface waves, below the Martian noise level as they are not observed in the InSight data. The considered marsquakes are comparable to tectonic earthquakes and characterized by high SNR and magnitude values of ~3. In addition, they are all located in the Elysium Planitia region and a majority of them are located on the Cerberus fossae system (from both MQS estimations by InSight Marsquake and Service, 2021 and by Drilleau et al, 2022).

The depth of the InSight events is an uncertain parameter and the current estimated values are notably between about 20 and 50 km (see Brinkman et al., 2021; Drilleau et al., 2022). Our results showed that it is possible to resolve the focal mechanisms in a stable manner along multiple depths for our entire dataset. In particular, we demonstrated for all events that there are the majority of the synthetic solutions that are compatible with the data surface wave amplitudes. More precisely, we found that the synthetic surface waves are an order of magnitude smaller than the Martian noise even at 12 km depth. Thus, this important result highlights the fact that seismic events can be shallow despite the absence of surface wave detection in the data. The depths of the events must also be consistent with the maximum detection depth of the secondary phases PP, SS, PPP and SSS in the synthetics, also identified in the seismic data (for instance in Khan et al, 2021; Drilleau et al, 2022). Therefore, we identified two solutions for each event; a first crustal solution between 12 and 24 km depth, and a second solution between 24 and 39 km depth. The two solutions were then related to the observations and geological knowledge of the region. We have identified several potential structures at the origin of the seismic events; the extensive Cerberus fossae and Grjotá Valles systems have been formed by deep massive dike networks (Ernst et al, 2001; Vetterlein and Roberts, 2010; Perrin et al, 2022) coupled with crustal weakening; the Martian wrinkle ridges, in particular those at Avernus Dorsa and Terra Cimmeria, are originated by the thermal contraction of the planet and are located at the apex of reverse faults at depth (Banerdt et al, 1982; Head et al, 2002); possible deep fractures without surface expression, related to the deformation of the dichotomy, from highlands to lowlands (Frey et al, 2002; Golombek et al, 2018; Pan et al, 2020).

We observed a majority of best moment tensor solutions that are at depths 18 km and 30 km for the nine marsquakes. Seven seismic events located on Cerberus fossae are in the same orientation (NE-SW) and with very steep nodal planes (60–80°). From our comparisons between morphology and moment tensor geometries, we concluded that S0173a, S0409d, S0809a and S0820a, which display normal faulting moment tensors, are presumably generated by subsurface normal faults, sub-parallel to the underlying dikes and to the grabens of Cerberus fossae. S0235b and S0484b, further north, are also extensive, and also related to the same seismic source type, *i.e.* related to normal fractures under Grjotá Valles certainly linked to dike propagations. Moreover, our results for events S0173a and S0235b are in good agreement with those presented in the companion paper by Brinkman et al. (2021). We both found extensive solutions for these events at similar depths of about 30–35 km. S0407a is reverse and likely result from the same faulting processes as those of S0173a, S0409d, S0809a and S0820a as the epicenters are close, but in a compressive context. S0784a is located on south lava plains, and its moment tensors in reverse regime are probably associated to a thrust fault below Avernus Dorsa, sub-parallel to the Martian dichotomy boundary. S0325a, the most distant event located on the dichotomy, is mainly reverse and possibly generated by compressive fractures related to the thermal contraction of the very old southern terrains. Our magnitude estimates are smaller than the MQS values (InSight Marsquake and Service, 2021) by a factor of ~0.5 for the nine marsquakes, while we agree with Brinkman et al. (2021) on their M_w estimations for S0173a and S0235b. Lastly, we also evaluated the quality factor Q which is not accurately known for Mars, however this parameter is the least constrained in this study and we could not deduce a value with confidence.

The InSight mission has been extended to the end of 2022. This would eventually lead to the detection of additional marsquakes in the vicinity of Elysium Planitia. An analysis on these new events would help to better understand the potential seismic sources, and how they can interact with each other. In addition, this work could be improved by addressing and resolving the main limitations we have mentioned. In particular, the structure models could be refined to take into account the lateral heterogeneities (mainly the depth of the Moho and the attenuation pattern) between the events and the landing site. And finally, continuous remote observations on structures (before and after quakes), for example from very high resolution HiRISE (McEwen et al, 2007) or CTX (Malin et al, 2007) images, would be very interesting to detect potential landslides related to marsquakes.

Declaration of Competing Interest

The authors declare that they have no known competing financial interests or personal relationships that could have appeared to influence the work reported in this paper.

Acknowledgements

We acknowledge NASA, CNES, their partner agencies and Institutions (UKSA, SSO, DLR, JPL, IPGP-CNRS, ETHZ, IC, MPS-MPG) and the flight operations team at JPL, SISMOC, MSDS, IRIS-DMC and PDS for providing SEED SEIS data. SEIS raw data are referenced at https://doi.org/10.18715/SEIS.INSIGHT.XB_2016. Funding support was provided by Centre National des Études Spatiales (CNES) and Agence Nationale de la Recherche (ANR-14-CE36-0012-02 SIMARS, ANR-19-CE31-0008-08 MAGIS, ANR-18-IDEX-0001 IdEx Université Paris Cité). The Mars Quake service (MQS) catalogues of seismic events used in this contribution are the Mars Seismic Catalogue, InSight Mission (V9 2022-01-01) available at https://doi.org/10.12686/a14 acknowledging ETHZ, IPGP, JPL, ICL, ISAE-Supaero, MPS, and the University of Bristol. The imagery data used in this study are available at the NASA PDS Imaging Node, for THEMIS, 2001 Mars Odyssey Online Data Volumes (https://pds-imaging.jpl.nasa.gov/volumes/ody.html) and MOLA, Mars Global Surveyor Online Data Volumes (https://pds-imaging.jpl.nasa.gov/volumes/mgs.html). This is InSight contribution number 240.

Appendix A. Supplementary data

Supplementary data to this article can be found online at doi:10.1016/j.tecto.2022.229434.

References

Aki, K., 1980. Scattering and attenuation of shear waves in the lithosphere. J. Geophys. Res. Sol. Earth 85 (B11), 6496–6504.

Aki, K., 1997. Seismic Coda Waves: A Stochastic Process in Earth's Lithosphere. Springer New York, New York, NY, pp. 1–24.

Andrews-Hanna, J.C., 2020. The tectonic architecture of wrinkle ridges on Mars. Icarus 351, 113937.

Banerdt, W.B., Phillips, R.J., Sleep, N.H., Saunders, R.S., 1982. Thick shell tectonics on one-plate planets: applications to Mars. J. Geophys. Res. Sol. Earth 87 (B12), 9723–9733.

Banerdt, W.B., Smrekar, S., Banfield, D., Giardini, D., Golombek, M.P., Johnson, C., Wieczoreck, M., et al., 2020. Initial results from the insight mission on mars. Nat. Geosci. 13 (3), 183–189.

Baratoux, D.H.S., Michaut, C., Toplis, M.J., Monnereau, M., Wieczorek, M., Garcia, R., Kurita, K., 2014. Petrological constraints on the density of the martian crust. J. Geophys. Res. Planet. 119 (7), 1707–1727.

Belleguic, V., Lognonné, P., Wieczorek, M., 2005. Constraints on the martian lithosphere from gravity and topography data. J. Geophys. Res. Planets 110 (E11).

Berman, D.C., Hartmann, W.K., 2002. Recent fluvial, volcanic, and tectonic activity on the cerberus plains of Mars. Icarus 159 (1), 1–17.

Böse, M., Clinton, J.F., Ceylan, S., Euchner, F., van Driel, M., Khan, A., Banerdt, W.B., et al., 2017. A probabilistic framework for singe-station location of seismicity on Earth and Mars. Physics of the Earth and planetary interiors 48–65.

Brinkman, N., Stähler, S.C., Giardini, D., Schmelzbach, C., Khan, A., Jacob, A., Nobuaki Fuji, Clement Perrin, Philippe Lognonné, Eric Beucler, Maren Böse, Savas Ceylan, Constantinos Charalambous, Clinton, J.F., van Driel, M., Banerdt, W.B., et al., 2021. First focal mechanisms of marsquakes. J. Geophys. Res. Planets.

Brown, J.R., Roberts, G.P., 2019. Possible evidence for variation in magnitude for marsquakes from fallen boulder populations, grjota valles, Mars. J. Geophys. Res. Planets 124 (3), 801–822.

Burr, D.M., McEwen, A.S., Sakimoto, S.E.H., 2002. Recent aqueous floods from the Cerberus fossae. Mars. Geophys. Res. Lett. 29 (1), 1–4.

Cabrol, N.A., Grin, E.A., Landheim, R., Kuzmin, R.O., Greeley, R., 1998. Duration of the Ma'adim Vallis/Gusev crater hydrogeologic system Mars. Icarus 133 (1), 98–108.

Carrier, A., Got, J.-L., Peltier, A., Ferrazzini, V., Staudacher, T., Kowalski, P., Boissier, P., 2015. A damage model for volcanic edifices: Implications for edifice strength, magma pressure, and eruptive processes. J. Geophys. Res. Sol. Earth 120 (1), 567–583.

Clinton, J.F., Giardini, D., Lognonné, P., Banerdt, B.W., van Driel, M., Drilleau, M., Murdoch, N., Panning, M., Garcia, R.F., Mimoun, D., Golombek, M., Tromp, J., Weber, R., B”ose, M., Ceylan, S., Daubar, I., Kenda, B., Khan, A., Perrin, L., Spiga, A., 2017. Preparing for InSight: An Invitation to Participate in a Blind Test for Martian Seismicity., 88, pp. 1290–1302.

Clinton, J., Ceylan, S., van Driel, M., Giardini, D., Stähler, S.C., Böse, M., et al., 2021. The marsquake catalogue from InSight, sols 0-478. Phys. Earth Planet. Inter. 310, 106595.

Crotwell, H.P., Owens, T.J., Ritsema, J., 1999. The taup toolkit: flexible seismic travel-time and ray-path utilities. Seismol. Res. Lett. 70, 154–160.

Dahmen, N.L., Clinton, J.F., Ceylan, S., van Driel, M., Giardini, D., Khan, A., et al., 2021. Super high frequency events: a new class of events recorded by the InSight seismometers on Mars. J. Geophys. Res. Planets 126 (2) e2020JE006599.

Drilleau, M., Samuel, H., Garcia, R.F., Rivoldini, A., Perrin, C., Michaut, C.M., et al., 2022. Marsquake locations and 1-d seismic models for mars from insight data. Earth Space Sci. Open Arch. 77.

Ernst, R., Grosfils, E., Mége, D., 2001. Giant dike swarms: Earth Venus, and Mars. Annu. Rev. Earth Planet. Sci. 29 (1), 489–534.

Fergason, R.L., Christensen, P.R., Kieffer, H.H., 2006. High-resolution thermal inertia derived from the Thermal Emission Imaging System (THEMIS): thermal model and applications. J. Geophys. Res. Planets 111 (E12).

Frey, H.V., Roark, J.H., Shockey, K.M., Frey, E.L., Sakimoto, S.E.H., 2002. Ancient lowlands on Mars. Geophys. Res. Lett. 29 (10), 1–4.

Fuji, N., Chevrot, S., Zhao, L., Geller, R.J., Kawai, K., 2012. Finite-frequency structural sensitivities of short-period compressional body waves. Geophys. J. Int. 190 (1), 522–540.

Fuji, N., Meschede, M., Konishi, K., Jaegler, H., Kawai, K., Zhao, L., Chevrot, S., Geller, R. J., Monteiller, V., Komatitsch, D., Calvet, M., Mizutani, H., 2016. DSM Kernel Suite. DSM. http://ipgp.github.io/DSM-Kernel/.

Geller, R.J., Ohminato, T., 1994. Computation of synthetic seismograms and their partial derivatives for heterogeneous media with arbitrary natural boundary conditions using the direct solution method. Geophysical Journal International 116 (2), 421–446.

Geller, R.J., Takeuchi, N., 1995. A new method for computing highly accurate DSM synthetic seismograms. Geophysical Journal International 123 (2), 449.

Genova, A., Goossens, S., Lemoine, F.G., Mazarico, E., Neumann, G.A., Smith, D.E., Zuber, M.T., 2016. Seasonal and static gravity field of Mars from MGS Mars Odyssey and MRO radio science. Icarus 272, 228–245.

Giardini, D., Lognonné, P., Banerdt, W., Pike, W., Christensen, U., Ceylan, S., Yana, C., 2020. The seismicity of Mars. Nat. Geosci. 13 (3), 205–212.

Golder, K.B., Burr, D.M., Kattenhorn, S.A., 2020. Investigation of target property effects on crater populations in long lava flows: a study in the cerberus region Mars, with implications for magma source identification. Icarus 335, 113388.

Golombek, M., Anderson, F., Zuber, M., 2001. Martian wrinkle ridge topography: evidence for subsurface faults from MOLA. J. Geophys. Res. Planets 106 (E10), 23811–23821.

Golombek, M., Grott, M., Kargl, G., Andrade, J., Marshall, J., Warner, N., Banerdt, W.B., 2018. Geology and physical properties investigations by the InSight Lander. Space Sci. Rev. 214 (5), 84.

Golombek, M.P., Warner, N.H., Grant, J., Hauber, E., Ansan, V., Weitz, C., Vrettos, C., 2020. Geology of the InSight Landing Site Mars. Nat. Commun. 11 (1), 1–11.

Grandin, R., Socquet, A., Doubre, C., Jacques, E., King, G.C.P., 2012. Elastic thickness control of lateral dyke intrusion at mid-ocean ridges. Earth Planet. Sci. Lett. 319-320, 83–95.

Guy, M.R., Patton, J.M., Fee, J., Hearne, M., Eric, M., Martinez, David, C., Ketchum, et al., 2015. National Earthquake Information Center systems overview and integration. US Department of the Interior, US Geological Survey Reston, VA.

Hamilton, C.W., Fagents, S.A., Wilson, L., 2010. Explosive lava-water interactions in elysium planitia, Mars: geologic and thermodynamic constraints on the formation of the tartarus colles cone groups. J. Geophys. Res. Planets 115 (E9).

Hartmann, W.K., Neukum, G., 2001. Cratering Chronology and the Evolution of Mars. Springer, pp. 165–194.

Hauber, E., Bro, P., Jagert, F., Jodlowski, P., Platz, T., 2011. Very recent and wide-spread basaltic volcanism on Mars. Geophys. Res. Lett. 38 (10).

Head III, J.W., Kreslavsky, M.A., Pratt, S., 2002. Northern lowlands of Mars: evidence for widespread volcanic flooding and tectonic deformation in the Hesperian period. J. Geophys. Res. Planets 107 (E1), 1–29.

Henry, C., Woodhouse, J.H., Das, S., 2002. Stability of earthquake moment tensor inversions: effect of the double-couple constraint. Tectonophysics 356 (1), 115–124. Seismic Source Mechanism through Moment Tensors.

Horvath, D.G., Moitra, P., Hamilton, C.W., Craddock, R.A., Andrews-Hanna, J.C., 2021. Evidence for geologically recent explosive volcanism in Elysium Planitia. Mars. Icarus 365, 114499.

InSight Mars SEI Data Service., 2019. Seis raw data, InSight mission.

InSight Marsquake Service, 2021. Mars seismic catalogue InSight mission v7 2021-07-01.

InSight Marsquake Service, 2022. Mars seismic catalogue InSight mission; v9 2022-01-01.

Irwin III, R.P., Howard, A.D., Maxwell, T.A., 2004. Geomorphology of Ma'adim Vallis, Mars, and associated paleolake basins. J. Geophys. Res. Planets 109 (E12).

Jaeger, W.L., Keszthelyi, L.P., McEwen, A.S., Dundas, C.M., Russell, P.S., Athabasca Valles, 2007. Mars: a lava-draped channel system. Science 317 (5845), 1709–1711.

Jost, M., Herrmann, R., 1989. A students guide to and review of moment tensors. Seismol. Res. Lett. 60, 37–57.

Karakostas, F., Schmerr, N., Maguire, R., Huang, Q., Kim, D., Lekic, V., et al., 2021. Scattering attenuation of the martian interior through coda-wave analysis. Bullet. Seismol. Soc. Am. 111 (6), 3035–3054.

Khan, A., van Driel, M., B”ose, M., Giardini, D., Ceylan, S., Yan, J., Clinton, J., Euchner, F., Lognonné, P., Murdoch, N., Mimoun, D., Panning, M., Knapmeyer, M., Banerdt, W.B., 2016. Single-station and single-event marsquake location and inversion for structure using synthetic Martian waveforms. Phys. Earth Planet. Inter. 258, 28–42.

Kedar, S., Panning, M.P., Smrekar, S.E., Stähler, S.C., King, S.D., Golombek, M.P., Banerdt, W.B., 2021. Analyzing low frequency seismic events at Cerberus fossae as long period volcanic quakes. J. Geophys. Res. Planets 126 (4) e2020JE006518 2020JE006518.

Khan, A., Ceylan, S., van Driel, M., Giardini, D., Lognonné, P., Samuel, H., Banerdt, W.B., 2021. Upper mantle structure of Mars from InSight seismic data. Science 373 (6553), 434–438.

Knapmeyer, M., Oberst, J., Hauber, E., Wählisch, M., Deuchler, C., Wagner, R., 2006. Working models for spatial distribution and level of Mars' seismicity. J. Geophys. Res. Planets 111 (E11).

Knapmeyer-Endrun, B., Panning, M.P., Bissig, F., Joshi, R., Khan, A., Kim, D., Banerdt, W. B., 2021. Thickness and structure of the Martian crust from InSight seismic data. Science 373 (6553), 438–443.

Lognonné, P., Mosser, B., 1993. Planetary seismology. Sur. Geophys. 14 (3), 239–302.

Lognonné, P., Banerdt, W.B., Giardini, D., Pike, W.T., Christensen, U., Laudet, P., Wookey, J., 2019. Seis: Insight's seismic experiment for internal structure of Mars. Space Sci. Rev. 215 (1), 12.

Lognonné, P., Banerdt, W., Pike, W.T., Giardini, D., Christensen, U., Garcia, R.F., Zweifel, P., 2020. Constraints on the shallow elastic and anelastic structure of Mars from InSight seismic data. Nat. Geosci. 13 (3), 213–220.

Malin, M.C., Bell III, J.F., Cantor, B.A., Caplinger, M.A., Calvin, W.M., Clancy, R.T., Thomas, P.C., Wolff, M.J., 2007. Context camera investigation on board the Mars reconnaissance orbiter. J. Geophys. Res. Planets 112 (E5).

Mangold, N., Allemand, P., Thomas, P.G., 1998. Wrinkle ridges of Mars: structural analysis and evidence for shallow deformation controlled by ice-rich décollements. Planet. Space Sci. 46 (4), 345–356.

Mangold, N., Allemand, P., Thomas, P.G., Vidal, G., 2000. Chronology of compressional deformation on Mars: evidence for a single and global origin. Planet. Space Sci. 48 (12), 1201–1211. Mars Exploration Program.

Maxwell, T.A., McGill, G.E., 1988. Ages of fracturing and resurfacing in the Amenthes region. Mars.

McEwen, A.S., Eliason, E.M., Bergstrom, J.W., Bridges, N.T., Hansen, C.J., Delamere, W. A., Squyres, S.W., et al., 2007. Mars reconnaissance orbiter's high resolution imaging science experiment (HiRISE). J. Geophys. Res. Planets 112 (E5).

Menina, S., Margerin, L., Kawamura, T., Lognonné, P., Marti, J., Drilleau, M., Karakostas, F., et al., 2021. Energy envelope and attenuation characteristics of High-Frequency (HF) and Very-High-Frequency (VF) Martian Events. Bullet. Seismol. Soc. Am. 111 (6), 3016–3034.
Michael, A.J., 1987. Use of focal mechanisms to determine stress: a control study. J. Geophys. Res. Sol. Earth 92 (B1), 357–368.
Mocquet, A., 1999. A search for the minimum number of stations needed for seismic networking on Mars. Planet. Space Sci. 47 (3), 397–409.
Molnar, P., Sykes, L., 1969. Tectonics of the caribbean and middle america regions from focal mechanisms and seismicity. Geol. Soc. Am. Bullet. 80, 1639–1684.
Montési, L.G., Zuber, M.T., 2003. Clues to the lithospheric structure of Mars from wrinkle ridge sets and localization instability. J. Geophys. Res. Planets 108 (E6).
Neumann, G.A., Zuber, M.T., Wieczorek, M.A., McGovern, P.J., Lemoine, F.G., Smith, D. E., 2004. Crustal structure of Mars from gravity and topography. J. Geophys. Res. Planets 109 (E8).
Pan, L., Quantin-Nataf, C., Tauzin, B., Michaut, C., Golombek, M., Lognonné, P., Lucas, A., 2020. Crust stratigraphy and heterogeneities of the first kilometers at the dichotomy boundary in western Elysium Planitia and implications for InSight lander. Icarus 338, 113511.
Parro, L.M., Jiménez-Díaz, A., Mansilla, F., Ruiz, J., 2017. Present-day heat flow model of Mars. Scientific Reports, 7. Nature Publishing Group.
Pasckert, J.H., Hiesinger, H., Reiss, D., 2012. Rheologies and ages of lava flows on Elysium Mons. Mars. Icarus 219 (1), 443–457.
Perrin, C., Jacob, A., Lucas, A., Myhill, R., Hauber, E., Batov, A., et al., 2022. Geometry and segmentation of Cerberus fossae, Mars: implications for marsquake properties. J. Geophys. Res. Planets 127 (1) e2021JE007118.
Platz, T., Michael, G., 2011. Eruption history of the Elysium volcanic province. Mars. Earth Planet. Sci. Lett. 312 (1), 140–151.
Plesa, A.-C., Bozdag, E., Rivoldini, A., Knapmeyer, M., McLennan, S.M., Padovan, S., Tosi, N., Breuer, D., Peter, D., Stähler, S., Wieczorek, M.A., van Driel, M., Khan, A., Spohn, T., 2021. Seismic velocity variations in a 3d Martian mantle: implications for the InSight measurements. J. Geophys. Res. Planets 126 (6) e2020JE006755.
Plesa, A.-C., Knapmeyer, M., Golombek, M.P., Breuer, D., Grott, M., Kawamura, T., Lognonné, P., Tosi, N., Weber, R.C., 2018. Present-Day Mars Seismicity Predicted from 3-D Thermal Evolution Models of Interior Dynamics. Wiley Online Library.
Plescia, J.B., 2003. Cerberus fossae, Elysium Mars: a source for lava and water. Icarus 164 (1), 79–95.
Quinteros, J., Strollo, A., Evans, P.L., Hanka, W., Heinloo, A., Hemmleb, S., et al., 2021. The GEOFON program in 2020. Seismol. Soc. Am. 92 (3), 1610–1622.
Rivas-Dorado, S., Ruiz, J., Romeo, I., 2021. Subsurface geometry and emplacement conditions of a giant dike system in Elysium Fossae, Mars. J. Geophys. Res. Planets 126 (1), JE006512 e2020JE006512 2020JE006512.
Roberts, G.P., Matthews, B., Bristow, C., Guerrieri, L., Vetterlein, J., 2012. Possible evidence of paleomarsquakes from fallen boulder populations, Cerberus fossae, Mars. J. Geophys. Res. Planets 117 (E2).
Romanowicz, B., Mitchell, B., 2015. 1.25-deep earth structure: Q of the earth from crust to core. Treatise Geophys. 1, 789–827.
Sato, T., Hirasawa, T., 1973. Body wave spectra from propagating shear cracks. J. Phys. Earth 21 (4), 415–431.
Scholz, J.-R., Widmer-Schnidrig, R., Davis, P., Lognonné, P., Pinot, B., Garcia, R.F., Banerdt, W., et al., 2020. Detection, analysis, and removal of glitches from insight's seismic data from Mars. Earth Space Sci. 7 (11) e2020EA001317.
Schultz, R.A., 2000. Localization of bedding plane slip and backthrust faults above blind thrust faults: keys to wrinkle ridge structure. J. Geophys. Res. Planets 105 (E5), 12035–12052.
Smrekar, S., McGill, G., Raymond, C., Dimitriou, A., 2004. Geologic evolution of the Martian dichotomy in the Ismenius area of Mars and implications for plains magnetization. J. Geophys. Res. Planets 109 (E11).
Smrekar, S.E., Lognonné, P., Spohn, T., Banerdt, W.B., Breuer, D., Dehant, V., 2018. Pre-mission insights on the interior of Mars. Space Sci. Rev. 215, 72.
Smrekar, S.E., Lognonné, P., Spohn, T., Banerdt, W.B., Breuer, D., Christensen, U., Wieczorek, M., et al., 2019. Pre-mission insights on the interior of Mars. Space Sci. Rev. 215 https://doi.org/10.1007/s11214-018-0563-9.
Stähler, S.C., Khan, A., Banerdt, W.B., Lognonné, P., Giardini, D., Ceylan, S., Smrekar, S. E., et al., 2021. Seismic detection of the Martian core. Science 373 (6553), 443–448.
Stutzmann, E., Schimmel, M., Lognonné, P., Horleston, A., Ceylan, S., van Driel, M., Stähler, S., Banerdt, B., Calvet, M., 2021. The polarization of ambient noise on Mars. J. Geophys. Res. Planets 126 (1) e2020JE006545.
Sun, W., Tkalčić, H., 2022. Repetitive marsquakes in martian upper mantle. Nat. Commun. 13 (1), 1–9.
Tanaka, K.L., Scott, D.H., Greeley, R., 1992. Global Stratigraphy. Provided by the SAO/NASA Astrophysics Data System, pp. 345–382.
Tanaka, K.L., Robbins, S.J., Fortezzo, C.M., Skinner, J.A., Hare, T.M., 2014. The digital global geologic map of Mars: chronostratigraphic ages, topographic and crater morphologic characteristics, and updated resurfacing history. Planet. Space Sci. 95, 11–24. Planetary Geology Field Symposium, Kitakyushu, Japan Planetary Geology and Terrestrial Analogs.
Tauzin, B., Pham, T.-S., Tkalcic, H., 2019. Receiver functions from seismic interferometry: a practical guide. Geophys. J. Int. 217 (1), 1–24.
Taylor, J., Teanby, N.A., Wookey, J., 2013. Estimates of seismic activity in the Cerberus fossae region of Mars. J. Geophys. Res. Planet. 118 (12), 2570–2581.
van Driel, M., Ceylan, S., Clinton, J.F., Giardini, D., Horleston, A., Margerin, L., Banerdt, W.B., et al., 2021. High-frequency seismic events on Mars observed by InSight. J. Geophys. Res. Planets 126 (2), JE006670 e2020JE006670 2020JE006670.
Vaucher, J., Baratoux, D., Toplis, M.J., Pinet, P., Mangold, N., Kurita, K., 2009. The morphologies of volcanic landforms at central Elysium Planitia: evidence for recent and fluid lavas on Mars. Icarus 200 (1), 39–51.
Vetterlein, J., Roberts, G.P., 2010. Structural evolution of the northern Cerberus fossae graben system, elysium planitia, Mars. J. Struct. Geol. 32 (4), 394–406.
Warner, N.H., Golombek, M.P., Sweeney, J., Fergason, R., Kirk, R., Schwartz, C., 2017. Near surface stratigraphy and regolith production in southwestern Elysium Planitia Mars: implications for Hesperian-Amazonian terrains and the InSight lander mission. Space Sci. Rev. 211.
Watters, T.R., 1993. Compressional tectonism on Mars. J. Geophys. Res. Planets 98 (E9), 17049–17060.
Watters, R.T., 2004. Elastic dislocation modeling of wrinkle ridges on Mars. Icarus 171 (2), 284–294.